Design of CNT Embedded Adhesive Film for Sensing, Control, and Reinforcement of PZT Actuator/Sensor Networks in Multifunctional Composites During Cure

Final Report

December 31, 2010

By

Giulia Lanzara, Lunwei Zhang, and Fu-Kuo Chang
Department of Aeronautics and Astronautics
Stanford University, Stanford, CA 94305

fkchang@stanford.edu
Tel: (650) 723-3466

REPORT DOCUMENTATION PAGE

Form Approved
OMB No. 0704-0188

1. REPORT DATE *(DD-MM-YYYY)*	2. REPORT TYPE	3. DATES COVERED *(From - To)*
Dec 31, 2010	Final Report	

4. TITLE AND SUBTITLE

Design of CNT Embedded Adhesive Film for Sensing, Control, and Reinforcement of PZT Actuator/Sensor Networks in Multifunctional Composites During Cure

5a. CONTRACT NUMBER

5b. GRANT NUMBER

FA9550-07-1-0350

5c. PROGRAM ELEMENT NUMBER

6. AUTHOR(S)

Giulia Lanzara, Lunwei Zhang, and Fu-Kuo Chang

5d. PROJECT NUMBER

5e. TASK NUMBER

5f. WORK UNIT NUMBER

7. PERFORMING ORGANIZATION NAME(S) AND ADDRESS(ES)

Department of Aeronautics and Astronautics
Stanford University, Stanford, CA 94305
fkchang@stanford.edu
Tel: (650) 723-3466

8. PERFORMING ORGANIZATION REPORT NUMBER

9. SPONSORING/MONITORING AGENCY NAME(S) AND ADDRESS(ES)

Dr. B. L. ("Les") Lee
Program Manager for Mechanics of Materials & Devices
Air Force Office of Scientific Research
4015 Wilson Boulevard, AFOSR/NA, Room 713
Arlington, VA 22203-195

10. SPONSOR/MONITOR'S ACRONYM(S)

11. SPONSOR/MONITOR'S REPORT NUMBER(S)

AFRL-OSR-VA-TR-2012-0185

12. DISTRIBUTION/AVAILABILITY STATEMENT

Distribution A

13. SUPPLEMENTARY NOTES

14. ABSTRACT

Structures with the multifunctional capabilities of self-sensing, diagnostics, self-repair, and mitigation of damage have demonstrated many benefits and advantages over traditional structures, particularly in enhancing structural safety, reducing maintenance cost, and improving performance.
The sensor is the most fundamental building block element that is needed for multifunctional structures. The integration of sensors in a network into structures involves serious challenges and difficulties. Although significant progress has been made in recent years, the durability and reliability of sensor networks for covering large structures remain a challenge. This research is proposed to develop a nano-technology to enhance the sensor-structure bond strength.
We designed, characterized and tested a novel sensor-structure bond with the help of a composite nano-structured film. The key feature is the integration of oriented carbon nanotubes (CNTs) directly

15. SUBJECT TERMS

SHM, structural health monitoring, CNTs, carbon nanotubes, sensors, PZT, piezoelectric,

16. SECURITY CLASSIFICATION OF:			17. LIMITATION OF ABSTRACT	18. NUMBER OF PAGES	19a. NAME OF RESPONSIBLE PERSON
a. REPORT	b. ABSTRACT	c. THIS PAGE			Byung Lip Lee
				40	**19b. TELEPHONE NUMBER** *(Include area code)* 703 696 8483

Reset

Standard Form 298 (Rev. 8/98)
Prescribed by ANSI Std. Z39.18

Table of Contents

1. Summary

Structures with the multifunctional capabilities of self-sensing, diagnostics, self-repair, and mitigation of damage have demonstrated many benefits and advantages over traditional structures, particularly in enhancing structural safety, reducing maintenance cost, and improving performance.

The sensor is the most fundamental building block element that is needed for multifunctional structures. The integration of sensors in a network into structures involves serious challenges and difficulties. Although significant progress has been made in recent years, the durability and reliability of sensor networks for covering large structures remain a challenge. This research is proposed to develop a nano-technology to enhance the sensor-structure bond strength.

We designed, characterized and tested a novel sensor-structure bond with the help of a composite nano-structured film. The key feature is the integration of oriented carbon nanotubes (CNTs), directly grown or implanted on the sensor (PZT), into the adhesive. The integration of the epoxy with oriented CNTs shows a potential improvement in the shear strength by comparison to commercial adhesives. This is because the oriented CNTs in the interface play a major role in the failure mechanism slowing down fracture propagation. The thin adhesive layer that bonds piezoelectric (PZT) sensors/actuators to a hosting structure has not been quantifiably assessed thus far. However, the health of the bondline is known to be critical to guarantee the performance and reliability of the underlying structural health monitoring system (SHM).

In this report, an investigation is performed to access the health of the PZT's bondline by coating the silver paste electrodes of a standard PZT with a carpet of carbon nanotubes. The resulting carbon nanotube-coated PZT is called CPZT. Once bonded to a host structure, the bondline of a CPZT consists of a thin adhesive layer integrated with fully oriented CNTs along its entire thickness. The CNTs in the interface serve as nanosensors for bondline health monitoring. By monitoring the electrical resistance variations of the carbon nanosensors, it is possible to gather important information on the adhesive cure level during the curing process, as well as monitor the interface integrity. Tests were performed under static as well as fatigue loading conditions due to: (a) continuous PZT expansions and contractions, and (b) fatigue structural loadings up to structural failure. The results presented in this report are important, not only because they show that the CPZT allows monitoring of the bondline health of PZT sensors/actuators mounted on a metal structure—as is highly desirable in SHM systems—but also because these results unfold, for the first time, an insight into the physical phenomena that occurs in the PZTs bondline during the lifetime of an SHM system.

2. Introduction

The reliability and performance of aircraft structures and, more in general, of any existing structure, are affected by degradation during the lifetime. Many aircraft flying today have in fact exceeded their design-life. Degradation can be due to damage resulting from external conditions, to fatigue loadings [1], as well as to exposure to severe environmental conditions. The structures' safety and operational capability are seriously influenced by these factors, and their maintenance is today an important issue. Standard inspection techniques involve costly, complex, and time consuming procedures. Therefore, the need for an accurate, fast, and reliable monitoring system is increasing today.

Multifunctional structures and composites are considered the most recent approaches to improving the safety, performance and reliability of structures. These systems also have the potentiality to drastically reduce operational costs.

The diagnostic capabilities in multifunctional structure are performed by Structural Health Monitoring systems (SHM) with, e.g., piezoelectric (PZT) sensors/actuators networks, and integrated hardware and software. These systems are today considered among the most promising methods to determine the integrity of structures in real time. The network is usually built-in or surface bonded to the structure.
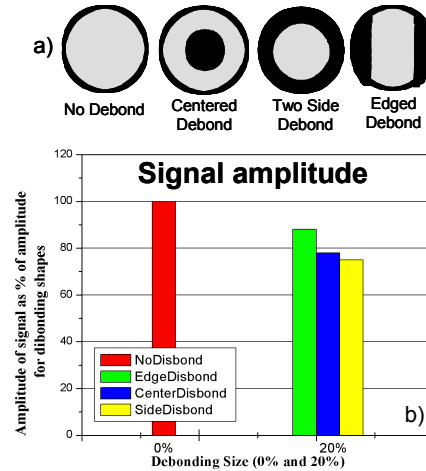
Figure 1. Amplitude dependence on the interface: a) Interfaces analyzed; b) maximum signal amplitude

A sensor network passive system is usually used for the identification of impact location and force history (Chang [2]). An active system consists of a sensor/actuator network and can be used for the detection of damage and residual strength.

This latter approach was used by Ihn and Chang [3] for the identification of invisible crack growth in aircraft structures. Piezoelectric ceramic discs (PZTs) are among the most widely used for SHM applications because they can serve both as sensors and actuators. By applying a pre-defined voltage to a PZT actuator, the ceramic disc expands/contracts, generating elastic waves that propagate into the structure. These waves are then captured by PZT sensors that transform them into electric signals. Finally, the generated signals can be interpreted in terms of damage location, size or material property changes. The interfacial adhesive layer that bonds the PZT sensors/actuators to a structure plays a critical role in the above described process; this is because it is through this layer that stress/strain is transferred from the PZT to the structure or vice versa. The dynamic interaction at the interface between these actuators and composites is critical for long-term applications.

The degradation of the interface can occur for mechanical or environmental reasons. The continuous electro-mechanical cycles of the PZT actuators can, over time, show interface degradation due to fatigue failure which causes interfacial crack propagation [4]. The mechanical properties and the integrity of the adhesive layer are crucial to achieve an efficient coupling between PZTs and the structure. We have, in fact, shown that the bondline properties during PZT adhesive curing [5] and a partial debond of PZT sensors/actuators from the structure [6] can cause phase and amplitude changes in the detected PZT signals, as shown in Figure 1. These changes, if not properly addressed, can negatively affect the performance and reliability of the underlying SHM system.

The problems are that: (a) currently there is no way yet that allows checking on the curing stage of the adhesive layer during the curing process, thus guaranteeing that the required mechanical properties are reached; (b) the cyclic PZT expansions and contractions, as well as the fatigue structural loadings, can cause severe bondline degradation (debond or cracks); and (c) the bondline integrity can only be detected with NDT techniques, such as X-ray and acoustic scanning which are extremely time consuming, especially in the case of large-scale sensor networks. They do not allow for monitoring of sensors embedded into structures, cannot provide any real-time information of the bondline, and cannot monitor the adhesive properties during manufacturing. Therefore, it is desirable to have a tougher adhesive bond and to be able to monitor, in real time, the adhesive properties as well as the bondline integrity.

The bond PZT-structure is usually achieved with the use of epoxies, which are the main cause of interfacial crack. A reinforcement of such bond would be the ideal solution. There are four main

requirements for the realization of an effective reinforcement: a) large aspect ratio, b) good dispersion, c) alignment, and d) interfacial stress transfer.

Carbon nanotubes (CNTs) [7] are the ideal candidate to reinforce materials thanks to their interesting mechanical properties and their very high aspect ratio. Recent developments in this emerging field has shown many promising results, particularly on polymer carbon nanotube composites (e.g. [8-21]). Recent use of soluble CNTs to enhance the mechanical properties of polymer composites has shown that with 10% MWNTs dispersed in a P(MMA-co-EMA), an improvement of 135% of Young's modulus and 49% of the tensile strength [8] was reached. The CNTs were also used to reinforce thermosetting polymers (such as epoxy) [22-25]. A 15% of adhesion strength was achieved with random CNTs to reinforce the interface between graphite fibers and resin in polymer composites [18]. Recently a 3D composite has been realized by growing CNTs forests on a fiber fabric layout [26].

However, dispersion and alignment of CNTs in the hosting matrix are still today the most important unresolved issues. To achieve a good load transfer, CNTs should be isolated and individually coated with the polymer. CNTs have tendency to aggregate due to their strong electrostatic interaction.

In this work we demonstrated a novel carbon nanotube (CNTs)-coated PZT (CPZT) [27] which represents a promising solution to the problems listed above, not only because this design allows for a stronger bondline that reduces the risk of interface degradation, but also because the CPZT design allows monitoring, over time, the bondline health in terms of adhesive curing and integrity under static as well as fatigue loading conditions. The results of this study are felt to be particularly significant because they allow, for the first time, access to the PZT's bondline first during fabrication, and then during the PZT's in-service life. This can lead to the development of more reliable SHM systems.

In this report we present a unique PZT- structure bond, its realization and mechanical testing. The interface consists on the integration of a pre-patterned high-density array of oriented CNTs into the bond. Two novel techniques were investigated and developed to directly grow or implant CNTs on the PZT surface. The presented approach overcomes the discussed problematic of dispersion and alignment of CNTs in the hosting matrix, giving as a result, a bond with enhanced mechanical performance.

3. Outline of the Work

In this report, first the CPZT design is presented, together with the description of the here-developed fabrication method. Finally, the multiple functionalities of the CPZT are demonstrated in terms of capability of the CNTs in the bondline to perform the following fundamental functions: (1) adhesive reinforcement [27] to enhance the bondline integrity over time; (2) electrode [28]; (3) adhesive cure monitoring during fabrication [29] ; and (4) adhesive integrity (debond/cracks or degradation) monitoring over time [29].

4. CPZT Design

In this investigation, the proposed is to develop a carbon nanotube coated piezoelectric (CPZT) actuator, where a high-density nano-electrode array of aligned carbon nanotubes (CNTs-NEA) replaces the silver paste electrode of standard PZTs and thus improves the bondline integrity. Figure 2 shows the schematic of the proposed CPZT design and a CPZT ceramic disc bonded to a substrate with a thin adhesive layer.

The resulting bondline consists of an adhesive layer fully integrated with oriented CNTs. The CNTs in the interface play the following fundamental roles (Figure 3), whose associated functions are, in practice. performed consistently in the following order: Step 1) adhesive cure monitoring during fabrication; Step 2) adhesive reinforcement to enhance the bondline integrity over time; and Step 3) monitor the adhesive integrity (debond/cracks or degradation) over time.
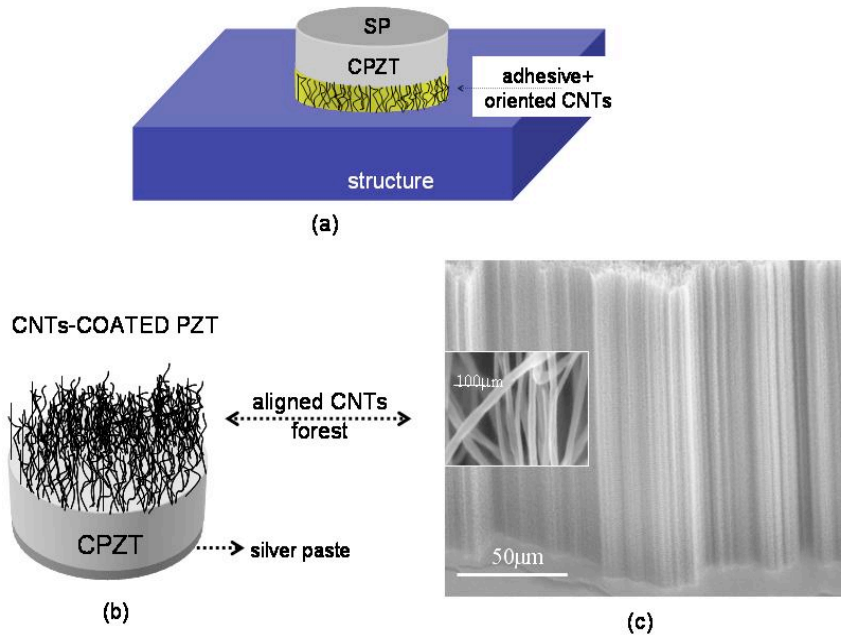
Figure 2. (a) CPZT bonded to a hosting structure, where the interface is integrated with a forest of aligned CNTs. (b) Schematic of the CPZT design, (c) Scanning Electron Microscope (SEM) image of a forest of aligned CNTs.

The CNTs in the interface are distributed in such a way to improve the interfacial shear strength of the bondline; this is because "shear" is considered to be the dominant action during cyclic expansions and contractions of PZT sensors and actuators. The concept at the base of the monitoring capability is that the CNTs in the bondline work as an array of carbon nanosensors which, being permanently integrated into the interface, can continuously monitor the bondline health in multiple stages (from fabrication to the entire in-service life). The functional key of the proposed approach is that the electrical resistance of the carbon nanosensors, measured between the metal plate and the silver paste electrode, is here demonstrated to be affected by both the adhesive properties during curing and by the bondline integrity.
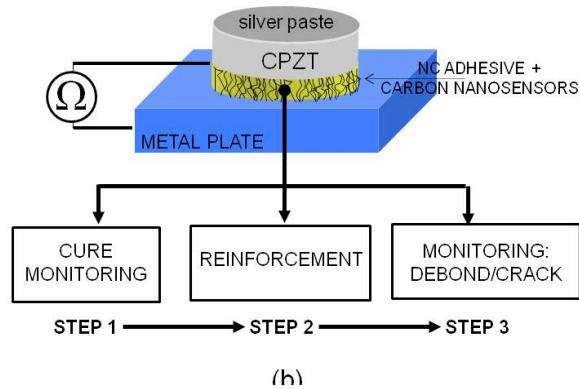

Figure 3. Fundamental functions.

5. CPZT Fabrication

In the interface design CNTs are uniformly dispersed and oriented in the adhesive polymer with their longitudinal axes perpendicular to the PZT surface. The main challenge in the fabrication process is the integration of uniformly dispersed and aligned CNTs into the ultra-thin adhesive interface (50μm to 100μm), and maintenance of electrical contact between the CNTs and the PZT surface.

Presented here is an approach that allows the integration of CNTs into the interface controlling their orientation, dispersion and distribution. The key element of the approach is to constrain a forest of aligned CNTs (CNTs-NEA) at its base (on the PZT surface or on the electrode surface) and integrate it into the adhesive polymer making use of the strong capillarity effect that characterizes the CNTs forest. In this way, the adhesive polymer is fully absorbed by the CNTs nanochannels [figure 4(b)], wetting each single CNT and maintaining its orientation; moreover CNTs migration and aggregation during the embedding and curing process is avoided because CNTs are constrained to the PZT surface. With this in mind, the first step is to coat the PZT surface with a high density array of aligned CNTs (forest), thereby constraining the CNTs tips to the PZT (C-PZT) as shown in figure 4(a). The next step is to drop a polymer adhesive onto the CNTs forest to bond the CPZT to a metal structure
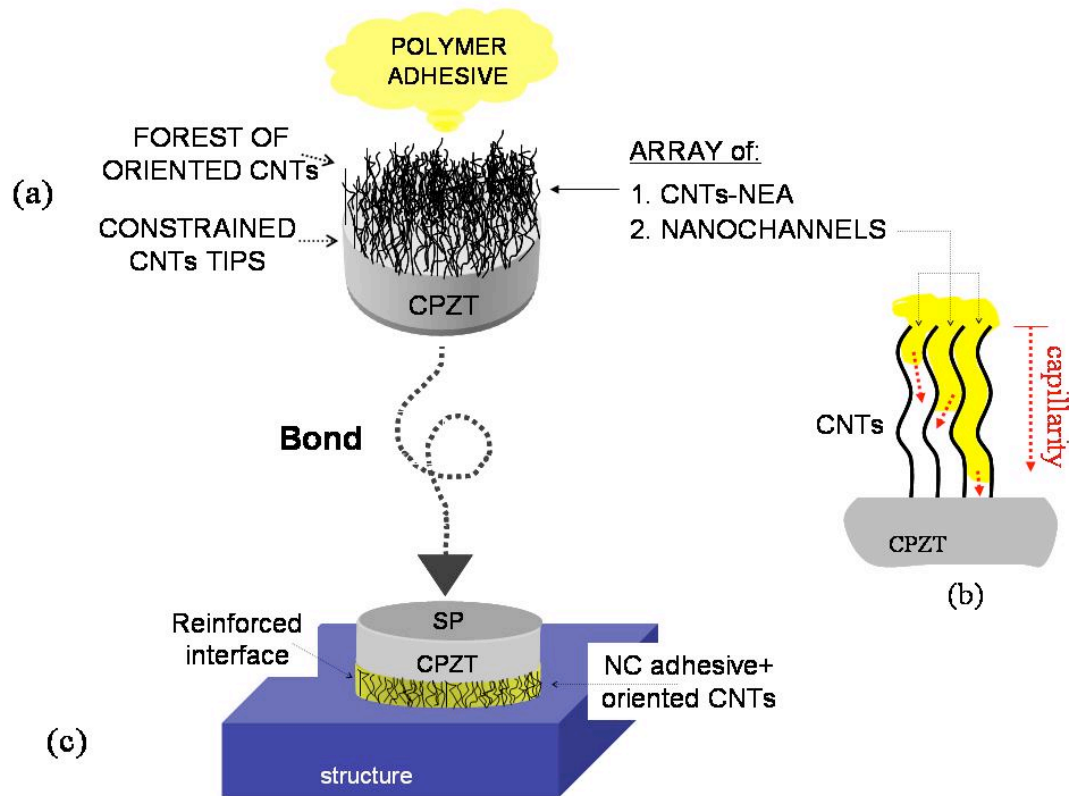
Figure 4. Scheme of the C-PZT design and fabrication approach
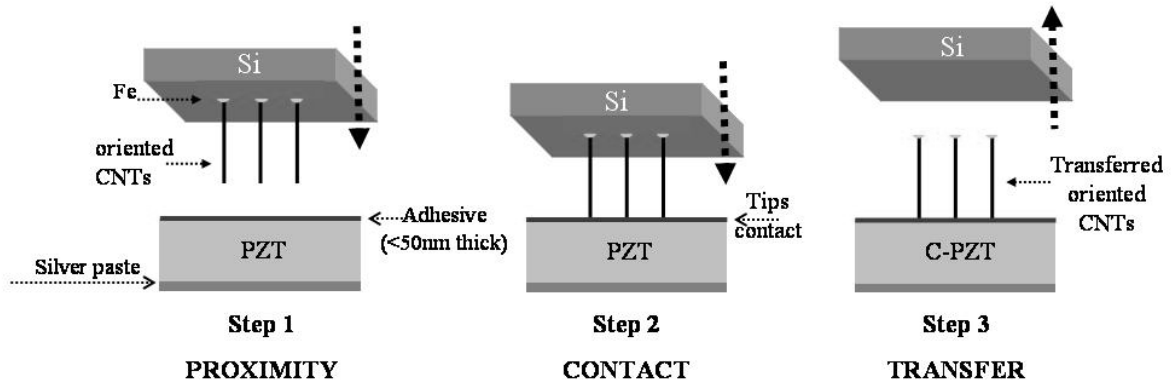
Figure 5. Transfer method

Here, coating is achieved by transferring a forest of oriented CNTs at room temperature from a substrate onto a polarized PZT or onto the silver paste electrode, with the help of an ultra-thin conductive adhesive layer. In this way electrical contact between the PZT and the forest of aligned CNTs is always maintained. A schematic of the process for the realization of the C-PZT is represented in figure 5 and later discussed.

This fundamental fabrication procedure has been adapted to the different studies that were performed to prove the various properties of the proposed CPZT design. Each procedure will later be discussed in detail.

6. Mechanical Characterization of the Interface

6.1 Fabrication process

Piezoelectric disks with silver paste electrodes were selected as the baseline PZT material. PZTs (material type 850) with diameters of 6.35mm and thicknesses of 250µm (t-PZT) and 750µm (T-PZT) were used. Several substrate types were investigated as shown in figure 6. The standard substrate is a PZT coated with the silver paste electrode. The second type is a bare PZT, and the third is a bare PZT coated with an Amorphous Silicon (AmSi) layer. The third substrate type was selected because it was shown [30] that an AmSi layer is needed to achieve direct growth of CNTs on a PZT surface. The influence of this layer on the mechanical response is investigated and compared with the CPZT design and fabrication method proposed in this report. The bare PZT is made by peeling off the original silver paste electrode. Peeling for T-PZTs is achieved via mechanical polishing using a diamond foil on a rotating plate, while for t-PZT it is achieved by etching the silver paste in a nitric acid bath. The etching process is chosen to avoid further and uneven PZT thinning. In this case only the SP electrode is brought into contact with the acid in order to minimize chemical variations in the PZT material. A 1µm thick AmSi layer was deposited with an e-beam evaporation system. Oriented multiwalled carbon nanotubes (MWNTs) were grown on a silicon chip with a Thermal Chemical Vapor Deposition (CVD) process, in a 50mm diameter horizontal quartz tube furnace. The silicon chip was first cleaned with Piranha and Hydrochloric Acid and then was coated with Iron (Fe) catalyst nanoparticles (24Å) through an e-beam evaporation system. Oxygen-free Argon was injected to purge the air in the furnace, and the temperature was increased and stabilized at a pre-set value (700°C) for 10 minutes. Ethylene gas was used as the hydrocarbon source which decomposed at high temperatures, forming a forest of oriented MWNTs on the Fe catalyst nanoparticles. Argon/Hydrogen was flowed prior to lowering the temperature to cool down the sample. As a result, the MWNTs were weakly bonded to the silicon chip.
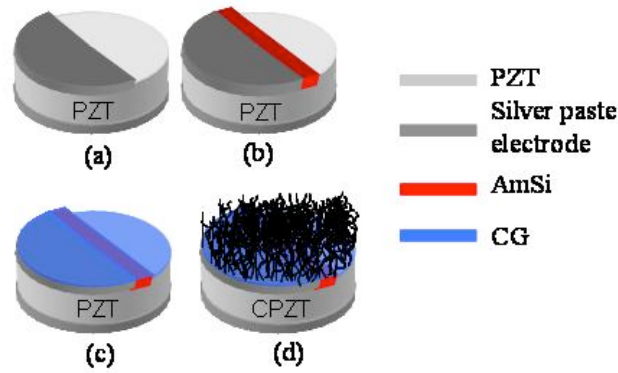
Figure 6. Process flow of the CPZT fabrication on different substrate types: (a) PZT peeling, (b) AmSi deposition, the figure showing the three substrates where CNTs were transferred for the mechanical study, (c) CG coating, (d) CNTs transfer

A conductive silver adhesive (CG) layer was spread onto the PZT surface and thinned down to 50nm-1µm [figure 6(c)]. The silicon chip, coated with the MWNTs forest, was reversed on top of the PZT substrate (or vice-versa) and the two parts were slowly brought into proximity with each other. As soon as contact was made, the Si chip was instantly removed, affecting the transfer of the MWNTs forest onto the PZT surface (figure 5). The samples design for the mechanical study required patterned CNTs coating on the PZT surface. This was achieved by patterning the CNTs forest either on the Si chip before CNTs transfer or directly onto the PZT surface after transfer. Patterning, before transfer, was achieved by growing CNTs only on pre-selected areas by selectively depositing Fe nanoparticles. This was done with the help of a shadow mask or with a standard photolithography process. Aligned CNTs were then grown on the patterned catalyst area. Patterning after transfer was achieved with a thin Kapton mask coated with a silicone layer that was brought into contact with the tips of the transferred CNTs forest and then lifted off.

After patterning, the CG layer was either cured at room temperature or cured on a hot plate for 10 minutes at 120°C. In this way the CNTs tips were constrained and electrically connected to the PZT substrate.

6.2 Sample design

An important aspect of this study is the design of the samples to be used to investigate the mechanical response of the bondline of a C-PZT surface mounted on a metal structure and to compare it with other bondline compositions. The major difficulty in this investigation was to test the shear strength of the C-PZT bondline avoiding PZTs failure due to their brittle nature. With this in mind, samples were designed in a way to avoid direct loading of the PZT ceramics, and to guide failure only in the CPZT/metal structure interface. Figure 7 shows a scheme of the proposed sample design where a PZT disc is fully bonded to a brass cube (10mm side) on one side and partially bonded to an iron (Fe) cube (2mm side) on the other side with Hysol EA9396 epoxy adhesive, which is a standard adhesive used in aerospace applications. The Fe cube is representative of the metal structure. The adhesive between the PZT and the Fe cube is reinforced with CNTs. With this design shear loads were applied directly to the Fe cube avoiding, as desired, direct loading of the PZT ceramic. Moreover, the smaller contact area between the PZT and the Fe cube guarantees that failure occurs in that interface only.
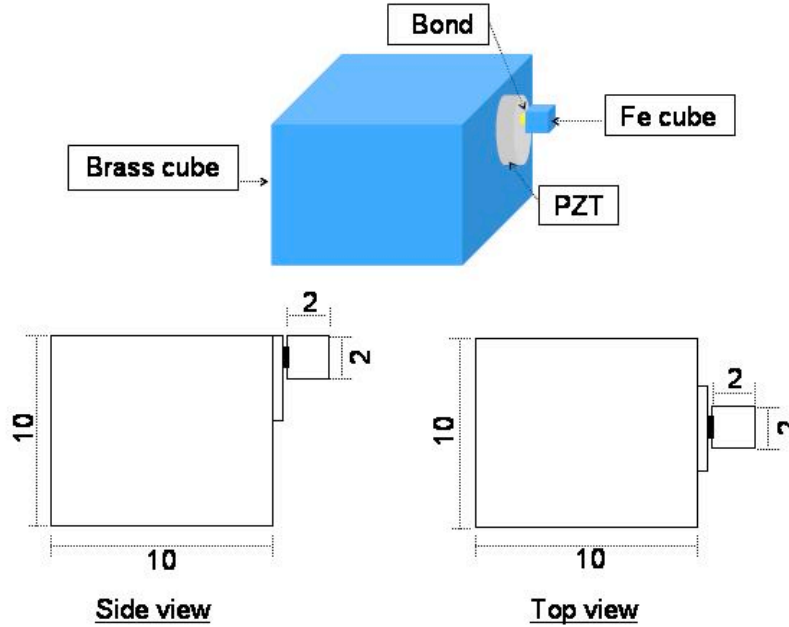
Figure 7. Samples design

The aim is to compare the following bondlines: (1) CPZT (with and without AmSi layer) bonded to the structure with the adhesive polymer, (2) a standard PZT surface coated with silver paste electrodes and bonded to the structure with the adhesive polymer, and (3) a bondline reinforced with randomly distributed CNTs in the adhesive polymer. For this reason, samples with three different PZT substrates and adhesive compositions were studied. The PZT substrates were: (1) standard PZT, (2) bare PZT, and (3) PZT coated with an Amorphous Silicon (AmSi) layer. The adhesive compositions were: (1) baseline adhesive (Type I), (2) adhesive reinforced with randomly mixed CNTs (Type II and III), and (3) adhesive reinforced with a high density array of oriented CNTs (CPZT) (Type IV). Sample types II and III differ in the volume of CNTs, which is equal to or twice that of the oriented CNTs case (Type IV). All 12 possible combinations of substrate types and adhesive compositions were studied for a total number of 43 samples.

6.3 Sample preparation

Samples were prepared by first bonding the Fe cube to the CPZT actuator and then bonding the PZT to the brass cube. Several challenges made the bonding process a difficult step: (1) contact area control, (2) bond thickness control, and (3) uniform dispersion and orientation of the CNTs in the hosting
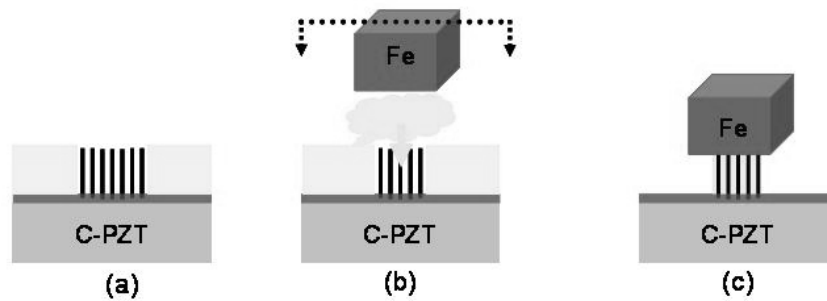
Figure 8. PZT metal bond procedure: (a) Teflon mask, (b) adhesive drop and metal position monitoring, (c) bond

adhesive. The approach is represented in figure 8. The contact area was controlled with a Teflon mask which was placed around the patterned forest of aligned CNTs (figure 8(a)). A small amount of adhesive was dropped onto the CNTs forest [figure 8(b)]. The Fe cube was mounted on a micro-manipulator, placed on top of the patterned CNTs and slowly brought into contact with the CPZT [figure 8(c)]. The bond thickness was controlled by controlling the vertical displacement of the micro-manipulator and by monitoring its gap from the PZT substrate. This method was also successfully used for large metal areas by mounting the PZT, rather than the metal, onto the micro-manipulator and by dropping the adhesive polymer onto the metal instead of the CPZT.
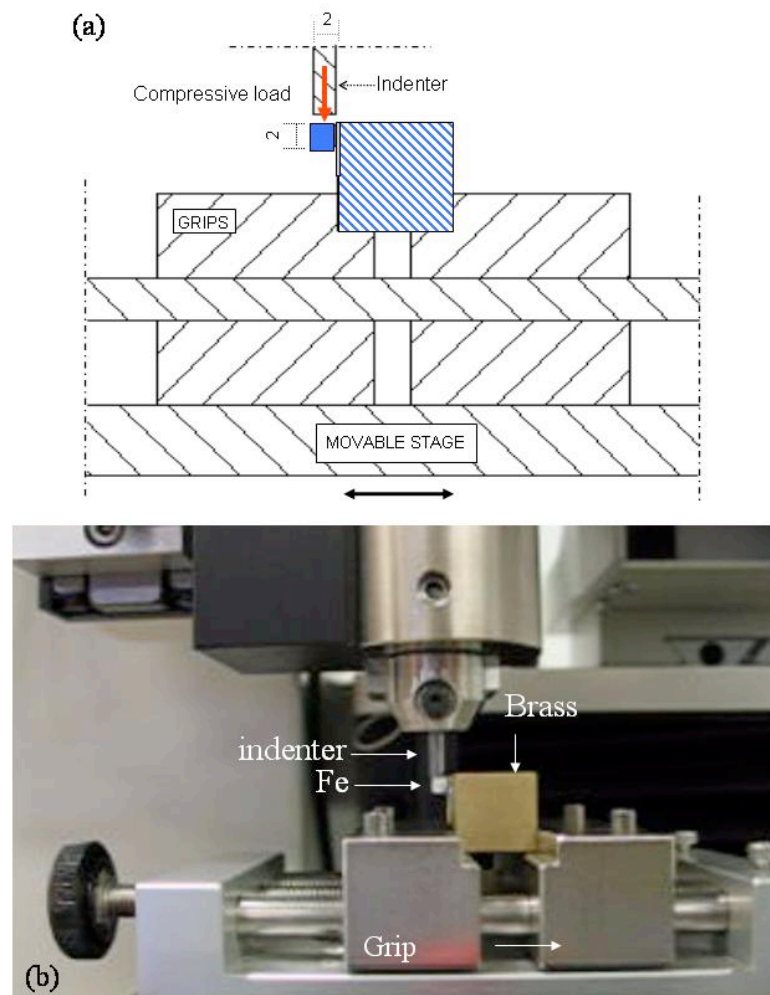
The interface reinforced with randomly mixed CNTs was fabricated by dropping a predefined volume of adhesive polymer onto a CNTs forest and by stirring the mixture with high energy. The mixture was then dropped onto the Teflon mask, which was mounted on the PZT surface prior to bonding the PZT to the Fe cube with the method previously described. The standard interface was built with the same fabrication process and using a standard adhesive polymer.
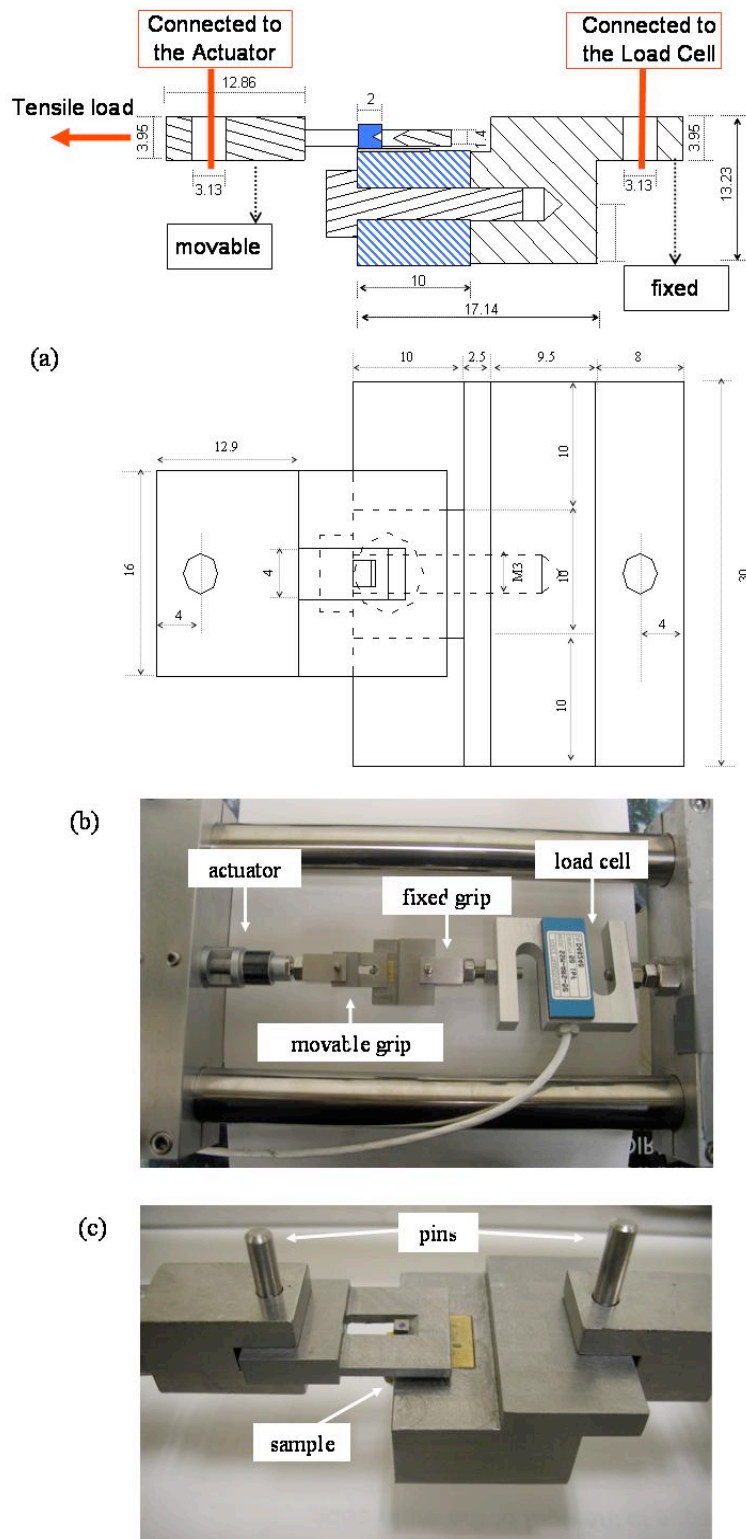
6.4 Testing fixtures

The primary goal of this work is to characterize the shear strength of the CPZT actuator bondline and compare it with that without CNTs (standard) and with randomly mixed CNTs. The major challenge is to measure the shear strength on a local scale for the very small interfacial areas involved. For this purpose, special test setups were chosen and adapted to this study by designing appropriate fixtures. The main idea is to perform tests by loading the interface, in shear, up to failure. A Micro Hardness Tester (MHT) and a Delaminator were chosen for this purpose. These instruments can apply low compressive and tensile loads and are mainly used for local analysis in very small areas. Figure 9 shows the MHT test setup. Typically an MHT consists of an indenter tip that can move in a vertical direction and apply a predefined load in compression. For this study, a 2mm diameter Tungsten Carbide (WC) flat indenter was designed in order to apply a uniformly distributed load to the Fe cube. The grip was part of a movable stage which allowed the control of the sample location along the horizontal plane.

The Delaminator setup is shown in figure 10. The setup consists of an actuator and a load cell placed along the same horizontal axis. The actuator can move to provide tension on the Fe cube sample while the load-cell, which is fixed at the other end and houses the sample, measures the load. Two special grips were designed and fabricated. The first grip was used to house the brass cube sample (see figure 10) with the help of a 3mm φ screw and to hold the interface in a horizontal plane during the test, parallel to the loading direction. The second grip was used to apply a shear load to the Fe cube by bringing the inside edge of the grip into direct contact with the Fe cube during testing (as shown in figure 10). These special grips are connected to the load cell and the actuator respectively with the help of 4mm pins which allow rotation of the grips around the pins' axis during testing (see figure 10).

Figure 9. MHT set-up: (a) scheme of the test, (b) picture of a sample during testing

Connected to
the Actuator

Connected to
the Load Cell

Tensile load

movable

fixed

(a)

(b)

actuator

fixed grip

load cell

movable grip

(c)

pins

sample

Figure 10. Delaminator setup: (a) scheme of the features design and test setup, (b) picture of the Delaminator components during testing, (c) higher magnification of the sample and test setup during testing

6.5 Test procedures

To characterize the bond shear strength of the PZT actuator interface, a shear load with increasing intensity and up to failure was applied to the Fe cube, while the sample was held in the mechanical grip of the MHT and in the load cell of the Delaminator. The failure loads were recorded and the shear strength of each of the tested samples was calculated by dividing the failure loads by the corresponding contact area. Contact areas were determined by means of scanning electron microscopy (SEM) imaging and characterization. In the case of the MHT setup, the Fe cube was placed under the flat indenter prior to testing. The indenter was brought into contact with the Fe cube with a contact force of 25mN and an approach speed of 40% per min. Upon contact, a compressive linear load (shear for the interface) with increasing intensity was applied to the Fe cube (loading rate of 15000mN/min) to bring the sample up to failure. In the Delaminator setup, the interface in analysis was kept in the horizontal plane parallel to the loading axis (actuator's axis). The inside edge of the grip, which was mounted onto the actuator (see figure 10), was brought into contact with the Fe cube. In this way, tensile loads (shear for the interface) were applied directly to the Fe cube until reaching failure. Tests were performed at an actuator speed of 0.27μm/sec.

6.6 Results and discussion

Here it is shown that the bondline strength of a CPZT surface mounted on a metal substrate is significantly improved in comparison with a PZT coated with standard silver paste electrodes. It is also shown that failure did not occur between the PZT and the oriented CNTs coating. In this study, emphasis is given to the bond shear strength, to the failure mechanisms, and to the influence on the failure mechanisms of the fibres length relative to the bond thickness (*Lc/H*). The analysis is also extended to different kinds of CNTs-reinforced interfaces, in order to understand how the adhesive composition, fibres orientation and dispersion influence the mechanical response. The next sections provide a step-by-step analysis and discussion of the developed CPZT fabrication process and the mechanical characterization.

6.6.1 CPZT fabrication

The electromechanical response of PZT actuators is related to the material elemental content (Lead-Zirconate-Titanate) and could be affected by acid treatments. Here are discussed the effects of the chemical treatment that was used to peel the silver paste (SP) electrode that coats standard PZTs. Particular focus is given to the elemental content and microstructure of the PZT material. The main result of this study is that nitric acid can be used to peel the SP electrode as shown by comparing the microstructure and elemental content of a treated and an untreated PZT. The analysis of XiRay Intensity vs. Energy (figure 10) shows that no meaningful variation in the *Ti* and *Zr* elemental content was observed in the case of treated PZT. These results were confirmed by the analysis of the PZT microstructure before and after treatment. A typical PZT morphology was characterized by a regular assembly of microscopic crystal grains (figure 11) which can still be recognized in PZT samples treated in nitric acid.

One of the advantages of the proposed CPZT fabrication method is that PZT depolarization is avoided due to the low temperature of the process. This method allows fabrication of a CPZT simply by transferring a forest of aligned CNTs directly onto a peeled and polarized PZT. The process results are shown in figure 11. A high density array of oriented CNTs were first grown on a Si chip [figure 12(a)] and then were transferred onto the PZT surface with the help of an ultra-thin CG layer. The CNTs' axes were oriented in the vertical direction, perpendicular to the Si substrate and were uniformly distributed over the entire surface. CNTs showed a homogeneous height and their longitudinal axes had a wave-like shape. Iron catalyst nanoparticles were mainly located at the tips in contact with the Si substrate showing a predominant bottom-up growth process. The free tips of the CNTs forest were then brought in contact with the PZT surface (coated with the CG layer). CNTs got transferred owing to the weak CNTs-Si bond and to the higher sticking force generated by the CG. Figure 12(b) shows an SEM image of a CPZT that is a polished PZT coated with a CNTs forest.
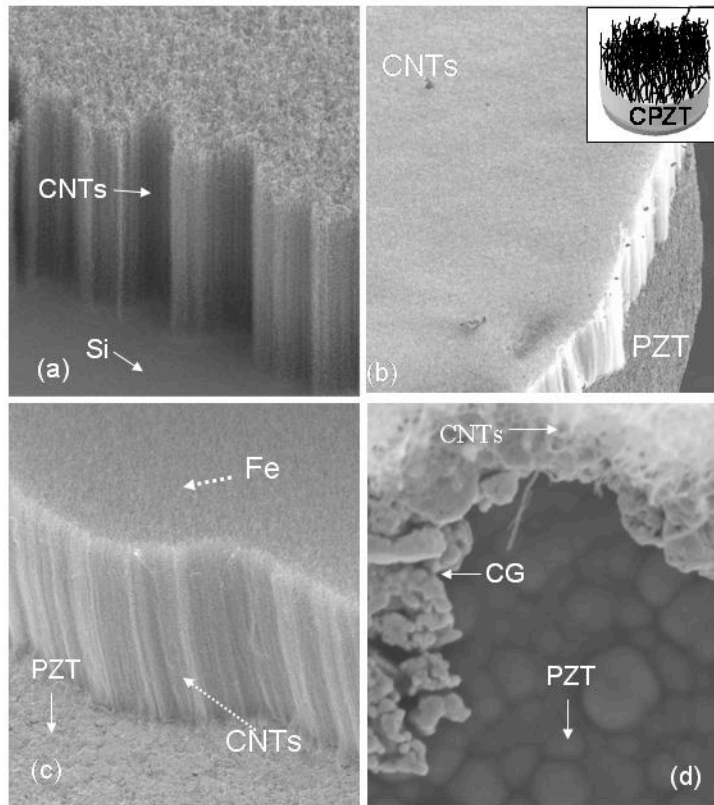
A higher magnification of the transferred forest is in figure 12(c). After the transfer, CNTs kept their vertical alignment and coated uniformly the entire PZT surface. Iron nanoparticles were then localized in the free CNTs tips and can be recognized in the image as the whiter dots. A scheme of the nanoparticles location is shown in figure 5. A top view SEM image of the edge of the CNTs forest is shown in figure 12(d).   Moving from the bottom to the top of the image the three overlapped layers are shown: (1) PZT grains, (2) conductive adhesive (CG), and (3) CNTs free tips.

The result of the transfer method shows that key elements for a successful transfer are the pressure applied during contact and the contact time. The pressure applied during transfer could compromise the result. CNTs are known to have, in compression, a very high deformability [30]. However, plastic deformations can occur for CNTs forests and these deformations may be localized at the CNTs tips for a low $Lc/\sqrt{A}$ ratio (Lc being the height of the CNTs and A a square extensional area of the forest) [30].
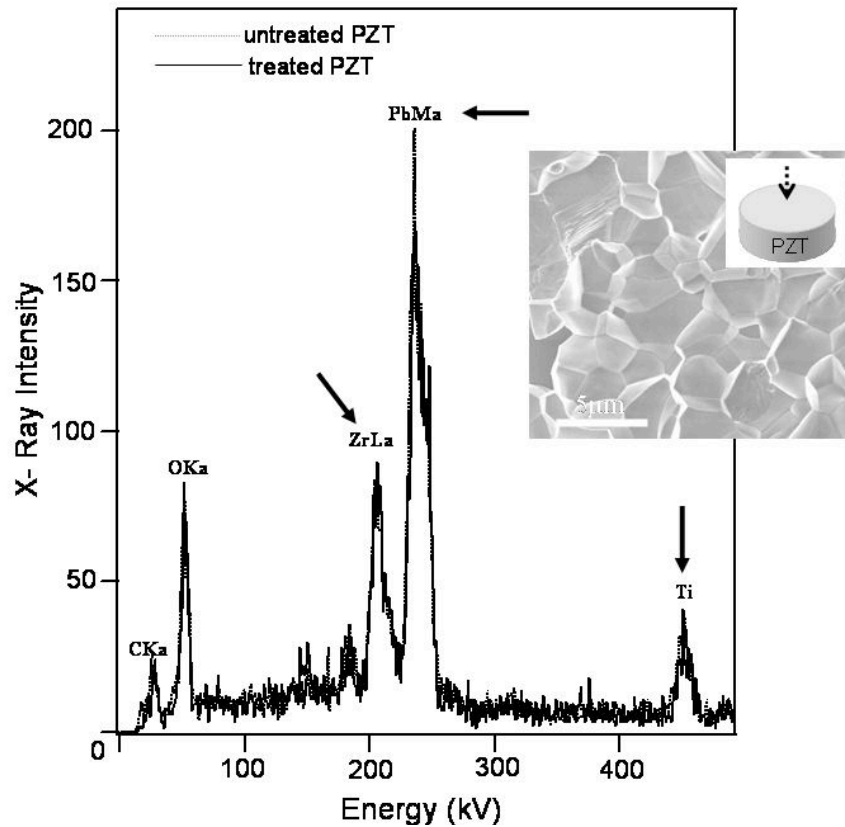
Figure 11. X-Ray Intensity vs. Energy for a treated and untreated PZT.
Inset: Scanning Electron Microscope (SEM) image of the PZT surface

Figure 13(a) shows an example of a CNTs forest, plastically deformed due to the pressure applied during transfer. The local deformation is usually uniformly spread all over the entire forest area (figure 13(a)).
The SEM image in the inset (left up) shows a higher magnification of a *kink*-like plastic deformation localized at the tips of the CNTs forest, as schematically represented in figure 13(a).

Figure 12. C-PZT fabrication results: (a) forest of oriented CNTs grown on a Silicon chip, (b) oriented CNTs forest transferred onto a bare PZT surface, (c) higher magnification of the transferred CNTs, (d) top view of the edge of the CNTs carpet. The image shows the PZT grains, the CG layer and the CNTs carpet

The contact time may influence the transfer result because the forest of aligned CNTs behaves as a high density array of nanochannels (figure 13(b)), being the average axial distance between each single CNT in the forest on the order of less than 50nm. The capillarity effect in a channel increases with the decreasing radius and so it is enhanced for the specific CNTs forest in analysis. As a consequence, when CNTs are brought into contact with a viscous fluid (like the non-cured CG), they may absorb the fluid along the nano-channels (along the forest thickness). A reduced contact time and a reduced thickness of the CG layer may reduce such an effect and enhance the transfer results. A longer contact time (order of 1sec.) could fully compromise the transfer. In this case, the forest of aligned CNTs would not be transferred onto the PZT; the forest would stay on the Si chip partially embedded in the CG. In figure 13(b) is an example of a CNTs forest, transferred onto the PZT surface and with a partial absorption of the CG along the forest thickness. CNTs forests were successfully transferred with conductive and nonconductive adhesive polymers, which lead to the adaptability of the proposed approach to different smart structures design
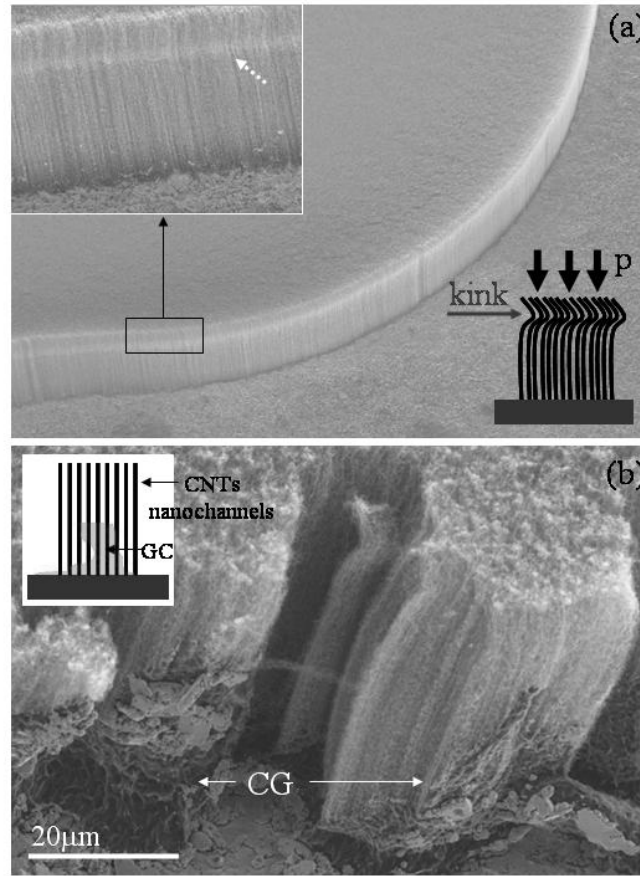
Figure 13. Key elements for the printing process: (a) plastic deformation due to excessive pressure (p), (b) CG absorption

6.6.2 Mechanical study

6.6.2.1 Samples preparation

Step-by-step results of the samples preparation are shown in figure 14. The sample design is such that only a small area of the PZT surface was bonded to the iron cube to avoid PZT failure during testing due to the brittle nature of PZT materials. This sample design leads to CPZTs that are coated with a patterned forest of aligned CNTs (figure 14a and 14b). The contact area between the CPZT and the Fe cube was controlled with a Teflon mask which was placed around the patterned forest (figure 14(c)).The CPZT was bonded to the Fe cube on the CNTs side (Figure 14(d)) by dropping the NC adhesive onto the transferred CNTs forest. The bond thickness was controlled by controlling the vertical displacement of a micromanipulator where the Fe cube was mounted. Samples with standard adhesive and with adhesive integrated with randomly dispersed CNTs were fabricated with the same procedure. However in the latter two cases the Teflon mask was mounted onto the PZT substrates to select the bond areas. The NC adhesive, with or without dispersed CNTs, was then dropped onto the confined area. The PZTs and the CPZTs were finally bonded to the brass cubes (Figure 14(d)). A picture of the samples prior to testing is shown in figure 14(e).
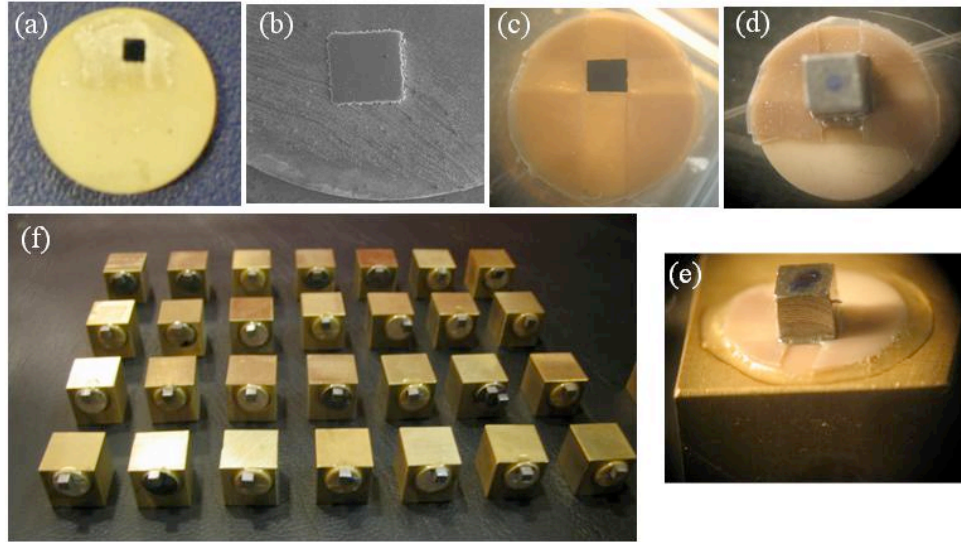
Figure 14. Samples preparation: (a) patterned oriented CNTs transferred onto the PZT surface, (b) SEM image (top view) of the patterned CNTs forest transferred onto the PZT surface, (c) Teflon mask to confine the CNTs area (the CNTs in the picture were patterned after being transferred onto the PZT), (d) iron cube bonded to the PZT, (e) PZT bonded to the brass cube, (f) example of the as fabricated samples (samples before testing)

6.6.2.2. Morphology of the CPZT bondline and comparison with other adhesive compositions

The goal of the CPZT design was to allow the "oriented" CNTs in the bondline to simultaneously play the role of reinforcing filler material and the role of electrode. Therefore, to optimize the performance and durability of the proposed CPZT interface, CNTs alignment along the interface thickness, CNTs dispersion into the hosting adhesive, and the electrical contact between the CNTs and the PZT are critical issues. With this in mind, a thorough microscopic analysis of the samples bondline was conducted to: (a) verify the CNTs dispersion in the adhesive, (b) determine whether the CNTs orientation was affected by the embedding process, (c) determine whether the CNTs were fully embedded into the polymer adhesive, and (d) verify if migration of CNTs happened during the curing process. The morphology of the resulting CPZT bondline was then compared with that of adhesives mixed with dispersed CNTs.

Figure 15 provides side views (SEM images) of a CNTs forest transferred onto a PZT surface (figure 15(c)) and then embedded into the adhesive polymer (figure 15(d)). These images show that CNTs kept their original wavelike configuration, alignment, orientation and location after being embedded into the polymer. The top view image of the same sample also shows (figure 15(d)) that each single CNT in the adhesive was isolated and surrounded by the polymer. This interesting result is due to the fact that: (a) the polymer was fully absorbed by the nanochannels along the entire channel length avoiding a direct loading of the CNTs due to the polymer weight, (b) the adhesive entirely filled up the nano-spaces along the CNT heights which avoided the formation of voids in the nanocomposite bond, and (c) the bond between the CNTs tips and the PZT surface avoided CNTs migration during the curing process. The final result was an adhesive reinforced with a high-density array of oriented CNTs which were fully dispersed and embedded in the hosting material and which were electrically connected [28] to the PZT surface. Transferring and constraining CNTs prior to embedding leads to an optimum result in terms of CNTs dispersion, uniformity and orientation.
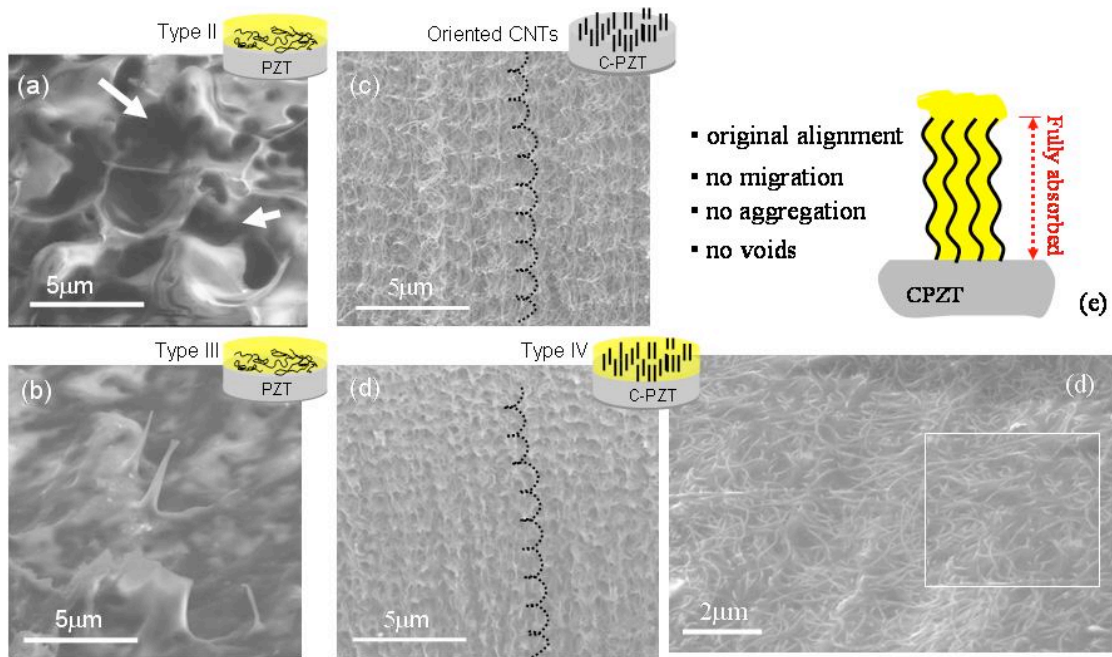
Figure 15. SEM images of the nanostructured bondlines used for the mechanical study: (a) adhesive mixed with random CNTs (Type II), (b) adhesive mixed with random CNTs (Type III), (c) side view of an oriented CNTs forest transferred onto a PZT surface (CPZT) before the embedding process. The wavelike configuration of the CNTs is highlighted. (d) side view of the CNTs forest (shown in (c)) embedded into the adhesive polymer (Type IV). After embedding, CNTs keep the same wavelike configuration (highlighted), (d) top view of the embedded CNTs forest, (e) schematic of the integration result for the case of oriented CNTs

The bondline morphology changes completely when CNTs are randomly mixed with the adhesive polymer (figure 15(a) and 15(b)). In this case CNTs tend to migrate inside the polymer and entangle during the mixing and curing process. The entangling effect is due to the CNTs' strong electrostatic attraction and is enhanced by the polymer flow at low viscosity during the high temperature curing process. This results in the formation of micro-agglomerates and of microdefects spreading all over the bond thickness (see arrows in figure 15(a)). The entangling effect increases with increasing CNTs volume fraction (figure 15(b)) leading to an ultra-viscous adhesive polymer layer prior to curing, and to an increase in agglomerates density over the bond thickness after curing. The surface of the adhesive polymer becomes rough because of microagglomerates sticking out in an irregular manner.

The mechanical response of the bondline was found to be strongly related to the adhesive morphology at the nano- and microlevel as discussed in the following sections.

6.6.2.3 Shear strength and the influence of CNTs orientation and distribution

The results of the normalized shear strength for each bondline type (Type I to Type IV) are reported in figure 16. The normalization is done with respect to the average shear strength of the baseline adhesive (Type I). The results clearly show that when CNTs are randomly mixed with the adhesive, the overall improvement of the shear strength is not significant compared to the baseline adhesive case (comparison of Type II and III with Type I). On the other hand, when oriented CNTs are used to reinforce the bond, a significant improvement of the shear strength is observed with a peak value of 274% (Type IV). In this case, however, the experimental results show a wide dispersion which seems to be attributable to the length of the CNTs relative to the bond thickness.

The shear strength results suggest that CNTs orientation and distribution inside the bond might be playing a major role. The test results were then interpreted with the help of an SEM analysis of the samples after failure. It was found that samples with different composition had different morphology at the nano- micro-scale (which confirms the results previously discussed) and that this difference influences the mechanical response of the bondline (figure (16)). The slight weakening of the bondline strength for samples Type II (20% CNTs volume fraction) is attributable to the micro-agglomerates and micro-defects that were found in the sample after failure. An enhancement in the weakening effect was observed for samples with a higher CNTs volume fraction (30% CNTs volume fraction). These samples where found, after failure, to be characterized by an increased number of micro-agglomerates and micro-defects all over the bond (Type III in figure (16)). When a forest of aligned CNTs is inserted into the adhesive polymer (CPZT case), CNTs are uniformly aligned and dispersed and this can lead to a significant improvement of the shear strength (Type IV in figure (16)). However the bondline strength was also found to be strongly related to other parameters. The analysis of both, the failure modes and the oriented CNTs microstructure inside the bond, allowed identification of these parameters and interpret the shear strength dispersion for the CPZT case (as discussed in the following sections).

6.6.2.4. Shear strength dependence on the oriented CNTs microstructure

Here it is shown that the length of the oriented CNTs relative to the bond thickness plays a major role in effectively reinforcing the bondline. To investigate the causes of the large variation of shear strength values in the case of oriented CNTs (shown in figure 16(a)), the oriented CNTs bond microstructures after failure were studied. Particular emphasis was given to the bond thickness (H) and the CNTs length (Lc).
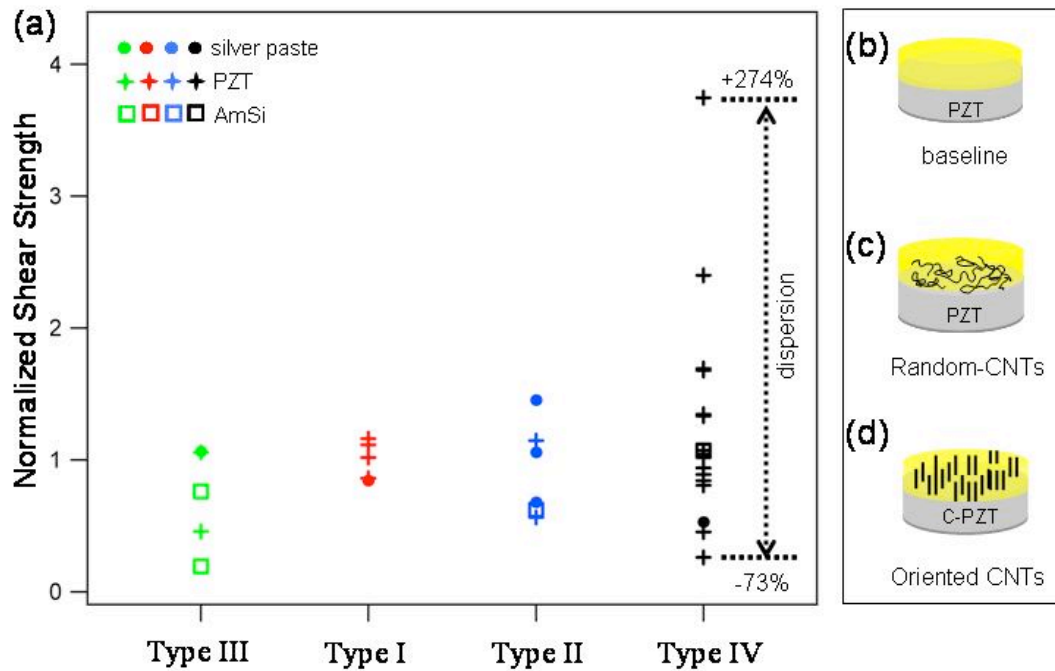
**Figure 16.** (a) Shear strength vs. adhesive composition, (b), (c) and (d) adhesive compositions
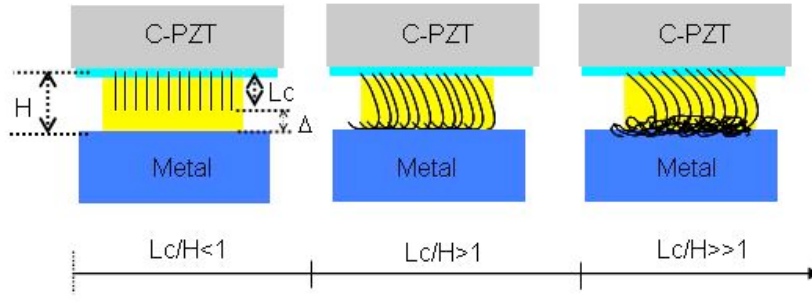
Figure 17. Different bondline microstructures for increasing *Lc*/*H* ratio

Three main microstructure types were identified and are schematically shown in figure 17: (a) oriented CNTs that are shorter than the bond thickness (*Lc/H<1*), (b) oriented CNTs that are longer than the bond thickness (in the range of *1< Lc/H<3*), or (c) oriented CNTs that are much longer than the bond thickness (*Lc/H>3*). When the oriented CNTs are shorter than the bond thickness, an adhesive layer reinforced with CNTs and of thickness *Lc,* is in direct contact with the PZT, while a very thin bare adhesive layer of thickness Δ is in direct contact with the metal surface (where Δ=*H–Lc*). When the oriented CNTs are longer than the bond thickness (*Lc/H>1*), the global and local deformation of the oriented CNTs forest is influenced by the bonding process. The CNTs tips in contact with the metal may locally fold, increasing the CNTs density in that region. As a consequence, the CNTs density along the bond thickness is non-uniform. In figure 18, the effect of the local deformation is shown for *Lc/H=1.1*. The forest of aligned CNTs after transfer and prior to embedding and bonding is shown in figure 18(a). In this case CNTs are vertically aligned. Once the adhesive is dropped onto the CNTs and the CPZT is bonded to the metal structure (Fe cube), the CNTs bend and their tips fold locally in the areas of contact with the metal. The typical example of a deformation is represented by the solid black line. Figure 18(c) shows a closer view of the folding effect at the metal interface.

The dependence of the folding effect on the *Lc/H* ratio is studied. The CNTs density and the folding effect at the metal interface increases with increasing *Lc/H* ratio (*Lc/H>>1*) as shown in figure 17. The density increase is found to lead, in extreme cases, to the loss of bond formation between the PZT and the metal structure. Two representative cases are shown in figure 19, left and right panels, for *Lc/H* = 1.2 and 3.6, respectively.

The folding effect is observed in both cases (see arrows in the upper panels), and appear to be stronger for the sample with the larger *Lc/H* ratio (right panels). For the 1.2 ratio value, the oriented CNTs are fully embedded and isolated from each other in the adhesive polymer layer while for the 3.6 ratio value, because of the larger folding effect, the resulting CNTs density at the adhesive/metal interface is larger, leading to partially exposed CNTs in that interface (top view picture in figure 19 – on the right panel).
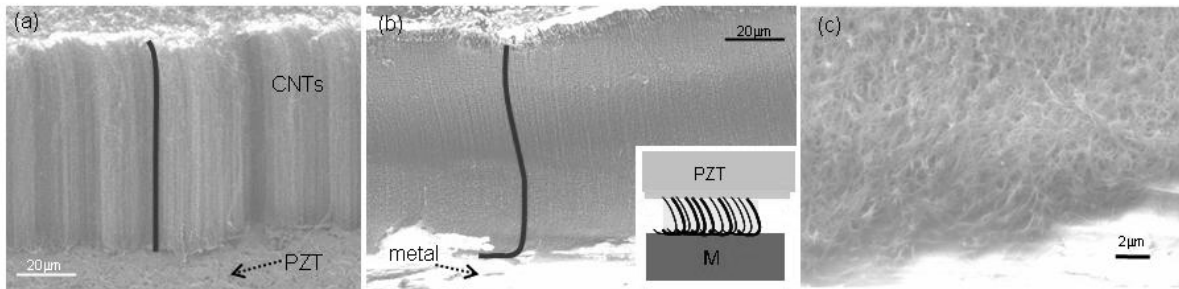
Figure 18. Bonding effect, SEM pictures: (a) PACNTs prior embedding, (b) side view of a bond, (c) folding effect. The sample has a ratio 1:1
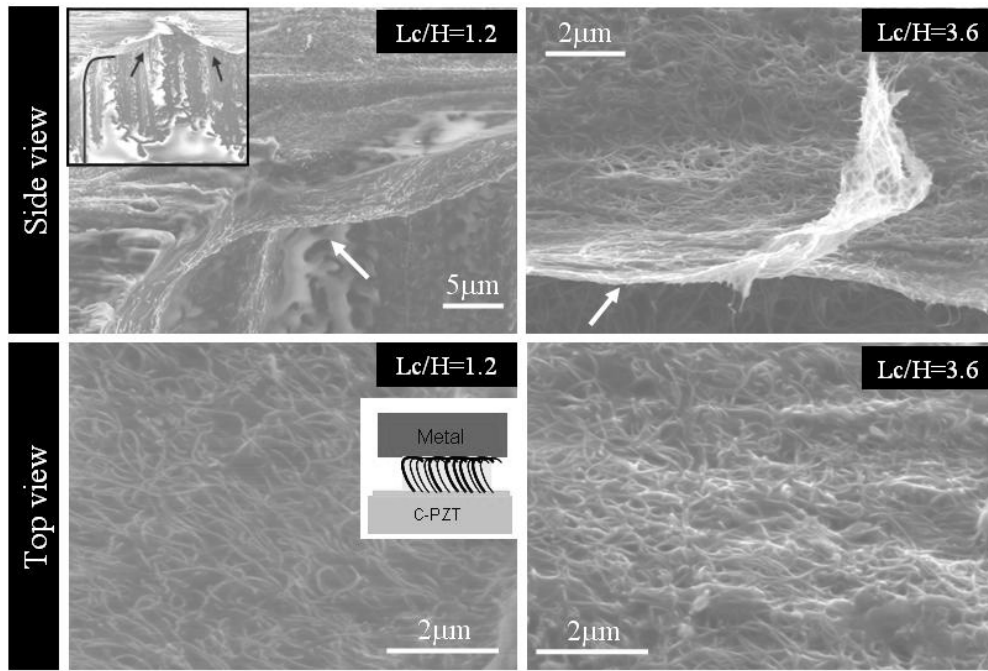
Figure 19. SEM images of the folding effect increase for higher Lc/H ratios

This microscopic analysis suggests that the variation of the *Lc/H* ratio leads to a non-uniform distribution of the CNTs along the bond thickness *H*. It is likely that this is the key aspect to explain the mechanical response of the PZT-metal bond.

6.6.2.5 Failure modes and their correlation with the interface microstructure

Here it is shown that bondline failure in the CPZT samples does not occur in the interface between the PZT ceramic and the oriented CNTs coating. However, it is shown that the bondline failure mechanisms and the shear strength are directly correlated to the *Lc/H* ratio. The dependence of the shear strength on the *Lc/H* ratio in the case of oriented CNTs is shown in figure 20. From the microscopic analysis of the failure mechanisms, a clear correlation is identified between the mechanical response and the adhesive layer microstructure discussed above.

More specifically, four different regions were identified corresponding to four different failure modes. These failure modes are found to be directly related to the *Lc/H* ratio, which gives rise to a different distribution of CNTs along the bond thickness, and hence to a different mechanical response. The direct relation between the mechanical response, the failure mechanisms and the geometry is schematically represented in figure 20 (ZONE I to IV). It is observed that when *Lc/H<1*, the failure occurs in the Δ layer (ZONE I of figure 20). When the ratio is *1<Lc/H<3*, there are two failure mechanisms (ZONE II and III): (a) cohesive failure involving the entire bond (ZONE II), or (b) failure of the support layers (ZONE III). Finally, all samples with *Lc/H>3* are characterized by an adhesive failure mechanism (ZONE IV).
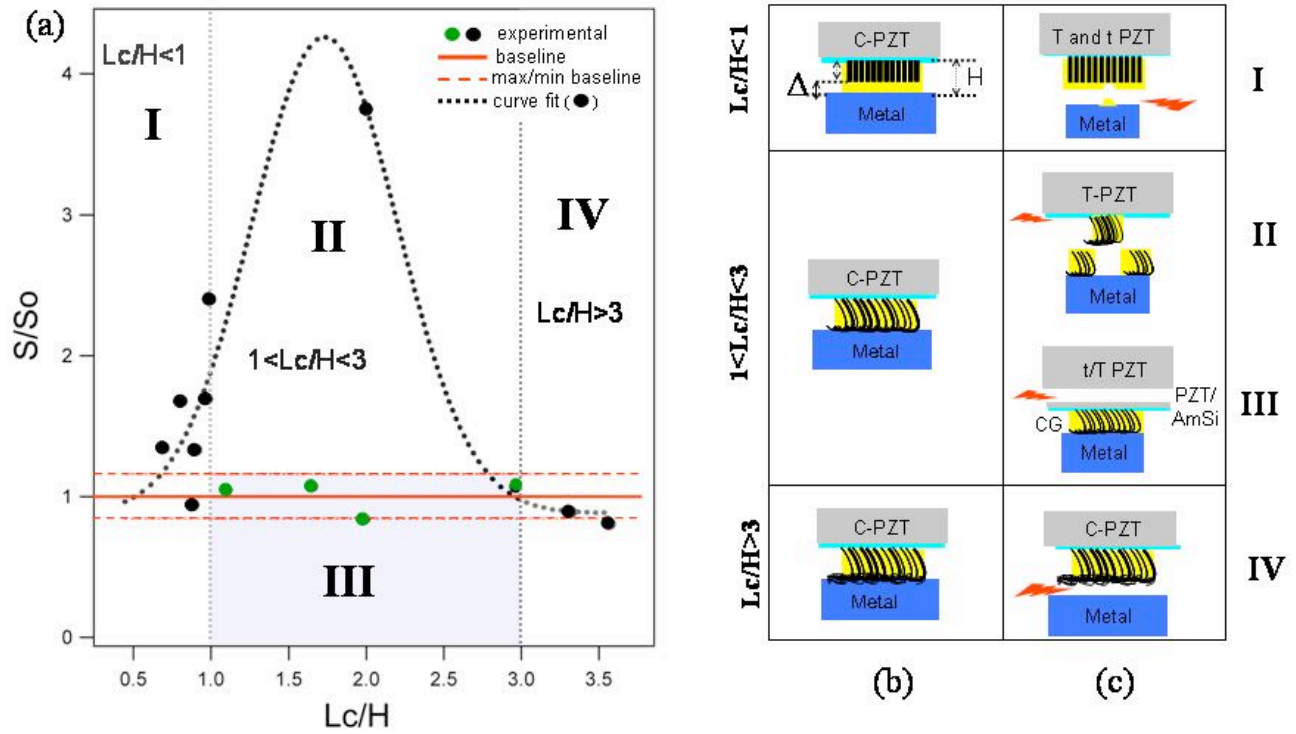
Figure 20. a) Normalized shear strength vs. *Lc/H*, (b) sample types, (c) failure modes corresponding to each sample type
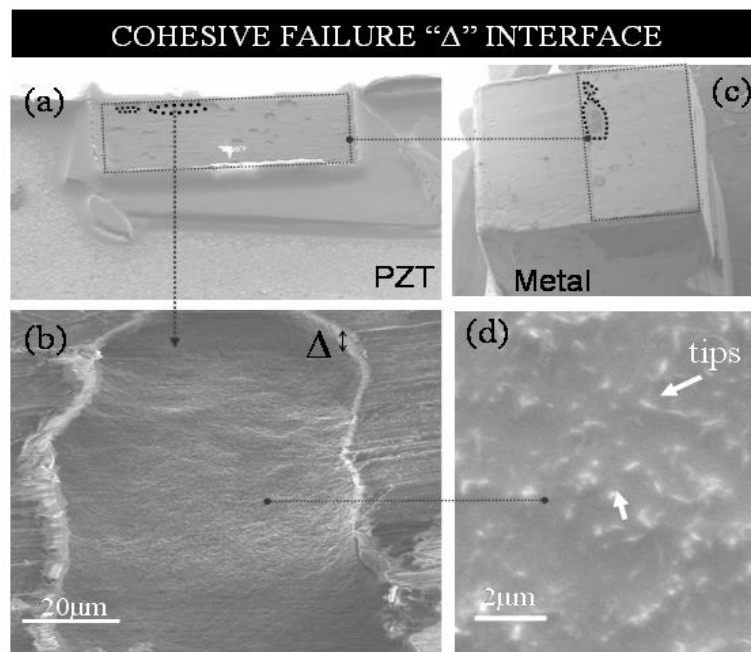

Figure 21. Cohesive failure for samples with *Lc/H*<1: (a) SEM image of the PZT surface, (b) fracture of the Δ interface, (c) iron cube, (d) higher magnification of the adhesive inside the fractured area.

When the oriented CNTs are shorter than the bond thickness, the bond is characterized by the layered microstructure previously described and schematically shown in figure 20(b) (ZONE I). In this case, cohesive failure is restricted to the top layer of thickness Δ (weaker bondline) above the CNTs leaving intact the CNTs layer below. An example of this failure mechanism is shown in figure 21. The highlighted zone represents the contact area between the PZT (figure 21(a)) and the metal (figure 21(b)) prior to failure. Adhesive polymer spots, as thick as the Δ layer, are found on the metal surface and are highlighted in the picture, while the bulk of the reinforced adhesive layer (thickness of Lc) is left on the PZT surface. A higher magnification of a hole on the PZT surface (figure 21(b)) shows the CNTs tips inside the adhesive polymer, which suggests that failure occurs in the Δ layer only.

Optimal results are observed when the oriented CNTs are longer than the bond thickness with Lc/H values between 1 and 3 (ZONE II). In this case, the bond is made up of a reinforced adhesive along its entire thickness (figure 20(b)), and the CNTs density in contact with the metal surface increases with the oriented CNTs length Lc. The highest shear strength improvement is observed when the CNTs length is twice as long as the bond thickness, and CPZTs are bonded to the metal cube. In this case multiple fractures along the entire bond thickness H and length are observed giving rise to cohesive failure of the interface. Figures 22(a) and 22(b) are SEM images showing the contact area between the PZT (figure 22(a)) and the metal surface (figure 22(b)) as highlighted. The multiple fractures are shown with the curves that are drawn for better visualization. Fractures in the PZT and metal particularly match each other. The fractured surfaces are mainly in multiple layers and orientations and have CNTs extending out of them (figure 22(c)). CNTs may slow down fracture propagation, keeping the edges of a propagating fracture (figure 23(b)) joined until their breaking and/or pull-out from the adhesive polymer occurs (figure 22(c)). On the other hand, when a fracture occurs in a baseline adhesive it rapidly propagates undisturbed in the bond until complete failure is reached (figure 23(a)). This behaviour can also be observed in the Displacement vs. Time curves (figure 23) of a bare and an oriented CNTs-reinforced adhesive which shows a failure delay if oriented CNTs are part of the bond.

When CNTs are much longer than the bond (ZONE IV), excessive folding of CNTs may weaken the interface in contact with the metal due to a much higher CNTs density in that interface. The density effect can be seen in figure 25(c) where the contact interface with the metal is shown. The shear strength is very low for all the analyzed substrates of this type.

The normalized shear strength (S/So) was plotted versus the Lc/H ratio by fitting the experimental data that showed an actual bond failure (zone I, II and IV). The resulting Gaussian fitting curve (figure 20) is representative of the mechanical response of the CPZT-metal bond as a function of the bond nano/microstructure (Lc/H). These results show that the Lc/H ratio is a key factor for truly reinforcing the bond shear strength with a high density array of oriented CNTs and could potentially be used to predict and design structural bonds with enhanced interfacial strength. A complete understanding of the observed phenomena is under investigation and more studies are being performed to control the bond thickness in relation to the CNTs length during manufacturing. The study of the long-term durability and signal analysis of the designed C-PZT sensor/actuator was studied and reported in [30].
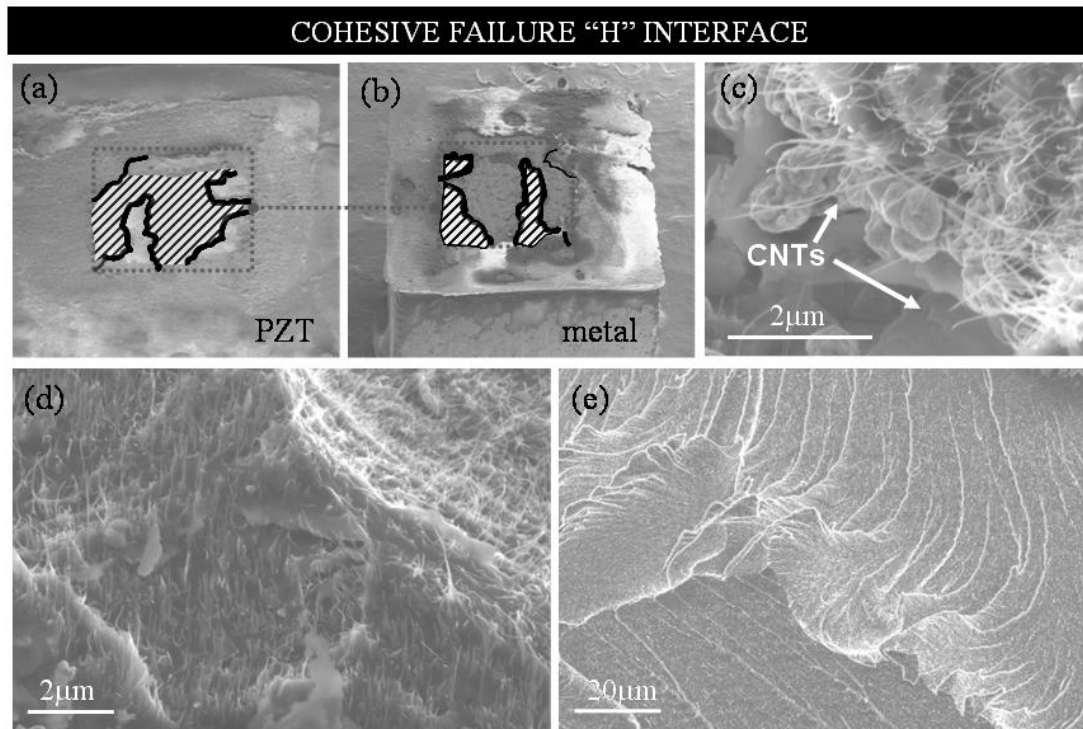
Figure 22. SEM images of a sample characterized by cohesive failure of the "*H*" interface: a) PZT surface, (b) metal surface, (c) CNTs tips sticking out of a fractured surface, (d) multidirectional fractured surfaces, (e) fractured surface
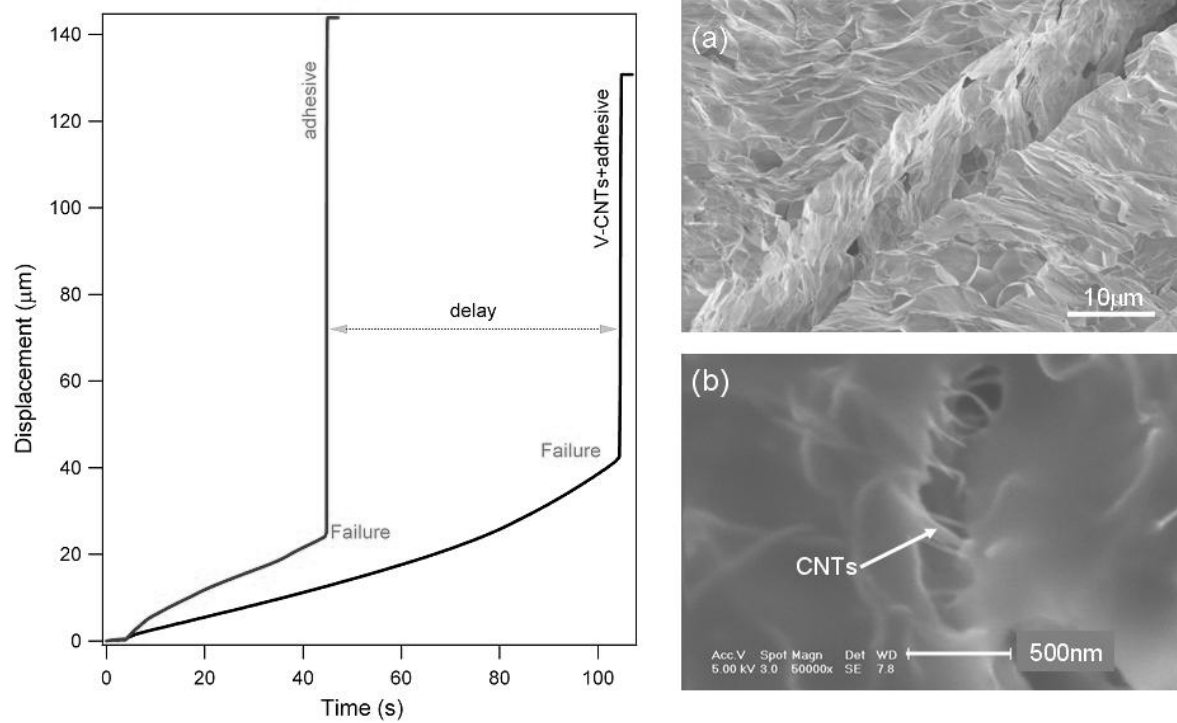
Figure 23. Displacement vs. time curve for a baseline adhesive and an adhesive integrated with vertically oriented CNTs. (a) SEM image of a fracture propagating in a baseline adhesive, (b) SEM image of a fracture propagating in an adhesive polymer integrated with CNTs
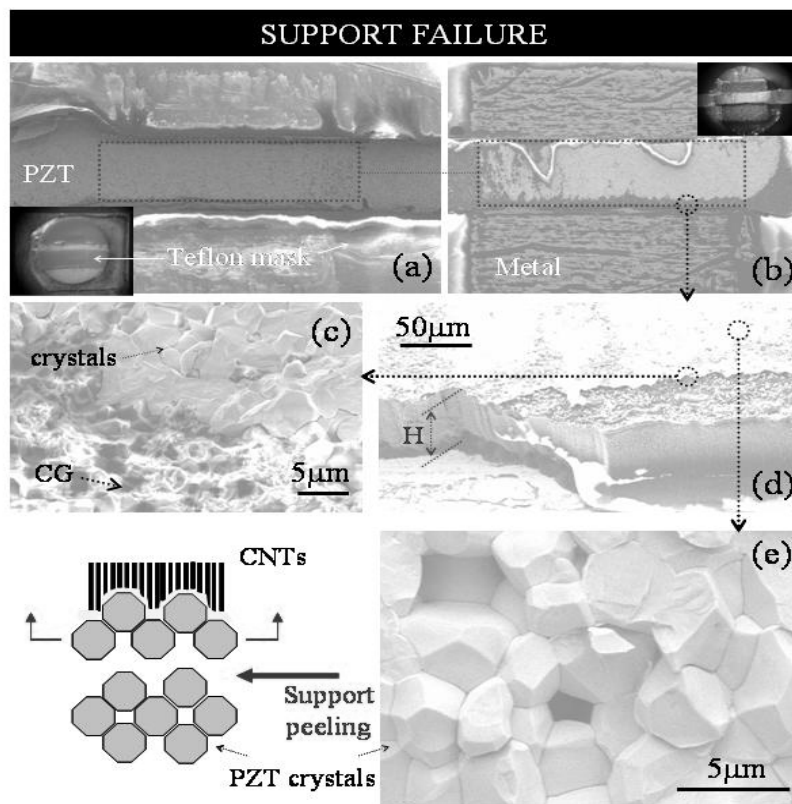
Figure 24. Support failure mechanism: (a) SEM image of the PZT surface, (b) SEM image of the metal surface, (c) top view of the interface in contact with the PZT (SEM image), (d) 45° view of the nanocomposite bond left on the metal surface (SEM image), (e) higher magnification of the PZT crystals peeled from the PZT substrate and scheme of the peeling mechanism (SEM image)
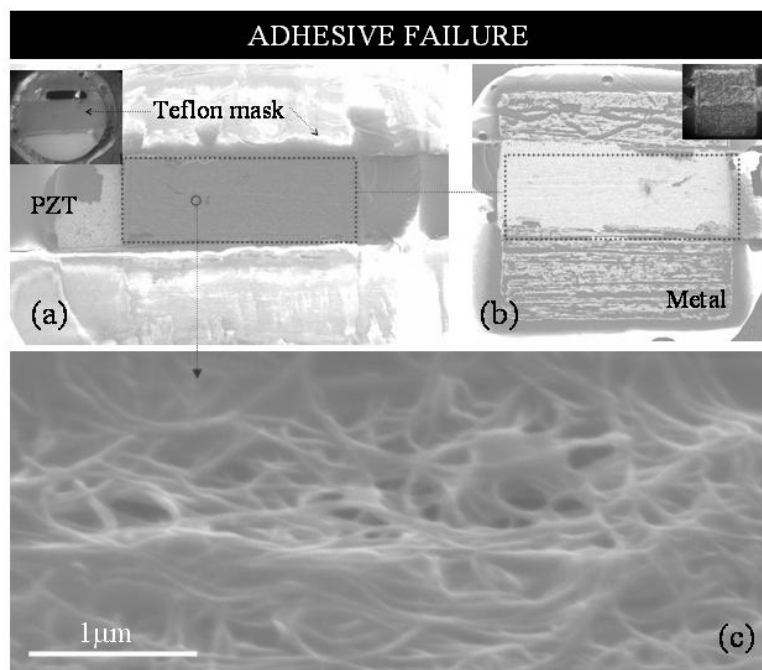
Figure 25. SEM images of the adhesive failure: (a) PZT surface, (b) metal surface, (c) contact interface metal-bond

7. Nano-Electrodes Study

Two nano-electrode designs were investigated in this study: (1) silver paste electrode (SP) coated with a forest of vertically aligned carbon nanotubes (CNTs) and; (2) a forest of vertically aligned CNTs. These electrodes were used to realize carbon nanotube-coated PZTs (CPZTs) by replacing one of the two SP electrodes of standard PZT transducers (shown in Figure 26(a)). A schematic of the CPZT designs and related electrodes can be viewed in Figure 26(b).
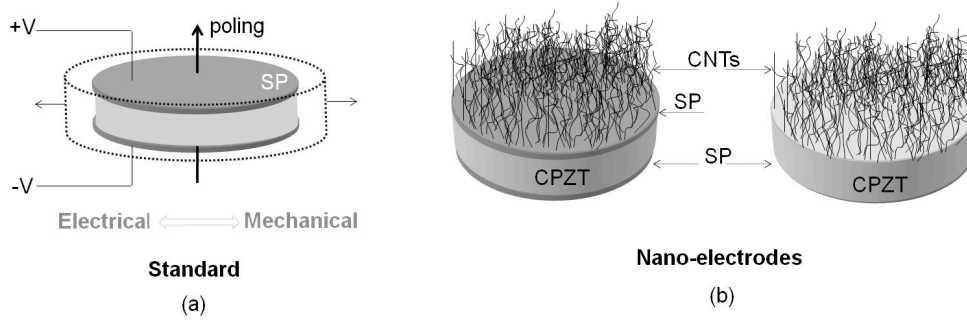
Figure 26. (a) Schematic of a standard PZT and its electro-mechanical behavior; (b) Schematic of the CPZTs designs and related nano-electrodes

The scope is to investigate the capability of the nanotubes to work as nanoelectrodes, study the effect of the nano-electrodes on the electro-mechanical response of PZT transducers under ultrasonic excitation frequencies and the electrodes response under the same frequencies. This is done by comparing the response of CPZTs and of standard PZTs. In practical applications PZT transducers are mechanically coupled to a substrate with the help of thin non conductive (NC) or conductive (CG) adhesive layers to allow for load transfer PZT/structure or viceversa. In the CG case the adhesive is additionally used to ground one of the PZT's electrode connected to it. The PZTs electro-mechanical response is known to be strongly influenced by the electrode efficiency as well as by the mechanical properties of the bond which can influence load transfer. PZT sensors/actuators in fact typically receive/induce the mechanical input through strain waves propagating in a structure. It is worth noting that the amplitude and phase of these waves can be affected by several factors (e.g. damping, temperature, structural imperfection or damage, mechanical behavior of the bond as well as its integrity) thus the PZT sensors might be subjected to different loading conditions and consequently would produce a different response that does not solely depend on the intrinsic response of the PZT actuator and of its electrode. The major problem is that all the aforementioned factors cannot be simply decoupled just by analyzing the output of PZTs mounted on a substrate. Decoupling these effects is important because CNTs-based electrodes are expected to have an impact on the electrical, mechanical and electromechanical response of the transducers once coupled to a substrate and each one of these contributions should be highlighted in the best possible way. For these reasons the nano-electrodes characterization is significantly challenging and the test designs are critical to properly address the physical response. With this in mind two test designs were implemented. First, a novel design (section 2.1) was proposed to solely investigate the effect of the nanotube electrode efficiency on the electromechanical response of the PZTs by avoiding any coupling with a substrate through the electrode and by avoiding the generation of a mechanical input through wave propagation, and then the mechanical coupling with the substrate was also taken into account (section 2.2) implementing a test setup that could allow strain waves to travel undisturbed in the substrate.

7.1. PZT stack design

Two PZTs were stacked one on top of the other as schematically shown in Figure 27 (picturing the CPZTs setup). The bottom and the top SP electrode of the PZTs were overlapped and bonded with a thin conductive (CG) adhesive layer which was electrically grounded (grounding the two electrodes in contact.
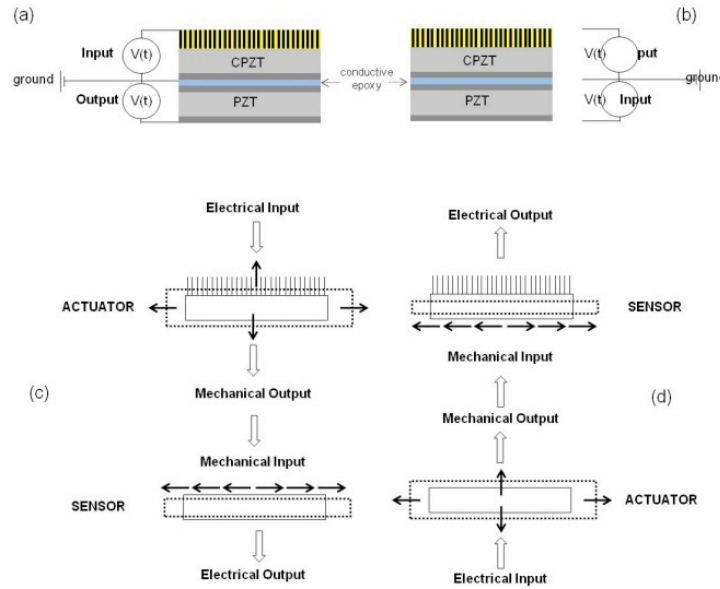

Fig. 27. (a), (b) Schematic of the stack PZT design for the actuation and the sensor study respectively; (c) and (d) schematic of the physics behind the proposed design

The electrode in analysis is the top electrode of the top PZT. Two different case studies were investigated to estimate the electrode efficiency in a sensing and in an actuating case. In the sensing case the bottom PZT is actuated by applying a voltage (electric input) to its bottom and top electrode and the output voltage (electric output) is detected between the electrodes of the top PZT. The actuating case pictures the process where the top PZT is actuated by applying a voltage to its top and bottom electrode (electric input) and the output voltage (electric output) is detected by the bottom PZT. The physics behind the proposed test setup for the actuating and the sensing case can be easily explained through the schematic in Figure 27(c) and 27(d) respectively. In the actuating case the PZT expands/contracts (mechanical output) upon application of an electrical input. This mechanical output is transferred (mechanical input) to the bottom PZT through the adhesive layer and the bottom PZT is driven to expand and contract generating charges among its electrodes (electrical output). In the sensing case the same physical process occurs, but in this case the electrical input is applied to the bottom PZT while the electrical output is recorded in the top PZT. The advantage of this design is that the direct contact between the two transducers guarantees knowledge of the mechanical input on the PZT sensors because any form of energy dissipation or waves distortion/changes are avoided. Moreover the electromechanical response of the PZT is purely devoted to the electrical efficiency of the electrode in analysis (top electrode of the top PZT) because effects such as bonding to a substrate, mechanical properties of the adhesive, do not play a role in this test setup.

Tests were performed on CPTZs (6.35mm diameter, 250mm thickness) with CNTs electrodes only (Figure 26b - right) to estimate the CNTs behavior and the results were compared with the case of standard PZTs (6.35mm diameter, 250mm thickness, and coated with a 6mm thick SP electrode). Sinusoidal input voltages characterized by a maximum pick-to-pick voltage of 200mV, 500mV, 800mV, 2V, 5V and with frequencies that ranged from 50 KHz to 750 KHz (step of 50 KHz) were applied by means of a signal generator, while output voltages were recorded through a SmartSuitcase (Acellent Inc.).
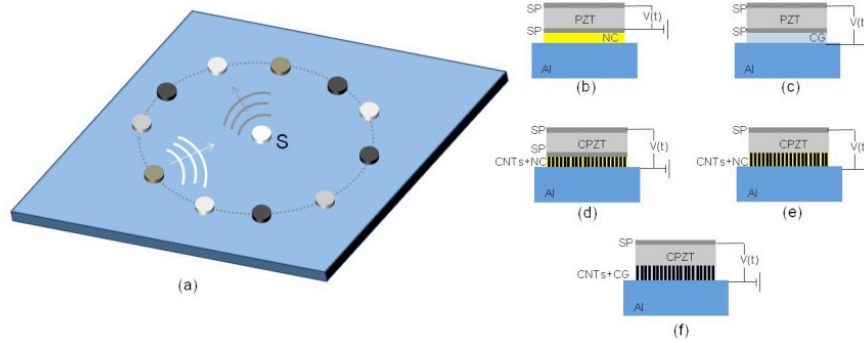
Figure 28. (a) Schematic of the test panel setup; (b)-(f) Samples under investigation and corresponding electrical wiring

7.2 Global characterization of the nano-electrode

The global electromechanical characterization of the nano-electrodes was studied through the test setup described in Figure 28 which allows taking into account not only the electrode efficiency but also the mechanical coupling PZT-structure thus the resulting resonance frequency of the PZTs/structure system and the consequent strain waves. The CPZTs and the standard PZTs under investigation (3.17mm in diameter) were surface mounted on a simply supported 3mm thick Al plate with the circular pattern (12cm in radius) shown in Figure 28a and were placed at a distance of 10cm from the edges of the plate to avoid boundary effects that can distort the propagating waves. A standard PZT (S) was mounted in the center of the plate. Two types of tests were performed to investigate the CPZTs response as sensors and as actuators. In the sensor study, the center PZT was actuated, generating strain waves that propagated in the plate in all radial directions. The strain waves were detected by the sensors (placed along the circle) and these output voltages were recorded and analyzed. In the actuator study the peripheral PZTs (CPZTs and standard) were individually actuated with the same input signal and the propagating waves were detected solely by the central sensor which generated an output signal for each of the actuators in analysis.

The major advantage of this test setup is that the PZTs are investigated with the same reference PZT and the induced waves (for both the sensor and the actuator case) travel the same distance. Moreover, amplitude and phase changes of the propagating waves due to temperature effects, damage in the structure or debond/cracks induced in the PZT interface are avoided because the test is performed under the same temperature conditions on an externally unloaded structure. As a consequence each sensor is actuated with the same signal in the sensor study and the signals generated by each peripheral actuator will be captured by the same PZT in the actuator study (avoiding different bonding conditions of the sensor that could affect the output voltage).

The CPZTs with the bottom electrode made of SP coated with the CNTs forest (Figure 26-left), were bonded to the plate with a non-conductive adhesive layer (Figure 28d), while the CPZTs with the bottom electrode made of a CNTs forest (Figure 26b-right) were bonded to the plate either with a conductive (Figure 28f) or with a non-conductive (Figure 28e) adhesive layer. Consequently three different nanostructured bonds were investigated. The CPZTs responses were respectively compared with standard PZTs bonded to the plate with a conductive (Figure 28c) or a non-conductive adhesive (Figure 28b). The reference PZT (S) was bonded to the structure with a conductive adhesive. The Al plate was electrically grounded, to directly ground the bottom electrode of all the PZTs bonded to the plate with the CG adhesive. The different wiring configurations for each sample type can be viewed in Figure 28b-28f. Five burst-input signals with a pick-to-pick voltage of 50V, and with frequencies that ranged from 200KHz to 900KHz (50KHz step), were used to actuate the PZTs. Input and output signals were generated/recorded with the ScanGenie (Acellent Inc.).

7.3 Fabrication process

Iron catalyst nanoparticles (24Å thick) were deposited on a pre-cleaned silicon wafer through an e-beam evaporation system. The wafer was cut in pieces and inserted in a chemical vapor deposition horizontal quartz tube furnace. First argon was flown in the tube to eliminate any residual oxygen, then temperature was increased up to 700ºC, and, once stabilized, Ethylene/Hydrogen were flown for the desired CNTs growth time. After a further injection of Argon, the sample was slowly cooled down. Meanwhile, one of the silver paste electrodes of standard piezoceramic discs (type 850, APC Inc.) was peeled-off, when necessary, by means of a room temperature nitric acid bath and was then rinsed in water.

A two parts silver paste adhesive (CG) was then used to manufacture the CPZTs by transferring the CNTs forest on the peeled PZT surfaces (Figure 26b-right) or on the PZTs SP electrode (Figure 26b-left) with the procedure described in Ref. [27]. Finally the samples were bonded to a standard PZT with a CG layer for the stack-PZT test setup and to the Al plate for the wave propagation study. In the latter case, a structural non-conductive adhesive (Hysol 9396) was additionally used to complete the entire set of samples, as previously described (Figure 3b-3f).

7.4 Results and discussion

A Scanning Electron Microscope (SEM) image of a fabricated carbon nanotube-coated piezoelectric ceramic disc (CPZT) can be viewed in Figure 29. In this case. CNTs are in direct contact with the PZT grains (the SP electrode was previously removed). The images clearly show the uniformity of the CNTs forest and the global directionality of the CNTs longitudinal axes. CNTs are 70µm thick with an average inter-tube distance (*d*) of approximately 50nm. The lower CNTs tips are permanently constrained to the PZT through an ultra-thin CG adhesive (5nm-10nm) which allow for charges transfer to take place at the CNTs/PZT grains interface, and also avoids loss of directionality and CNTs spreading during the adhesive curing process. The results can in fact be viewed in Figure 29(c) which shows an SEM image of the CNTs forest after being embedded in a NC adhesive. The image clearly shows that the CNTs are fully embedded in the adhesive and keep their original orientation after curing.
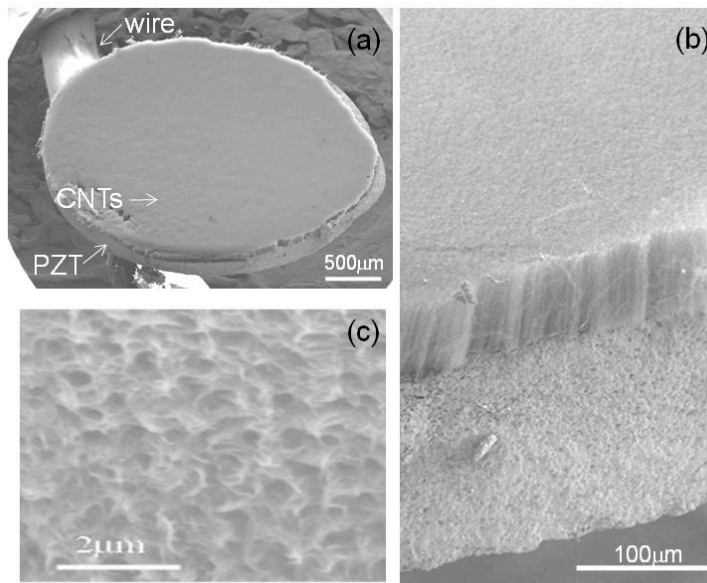

Figure 29. . SEM images of a fabricated CPZT; (b) Higher magnification to show the CNTs orientation and the forest uniformity; (c) SEM image of oriented CNTs embedded in a NC adhesive.
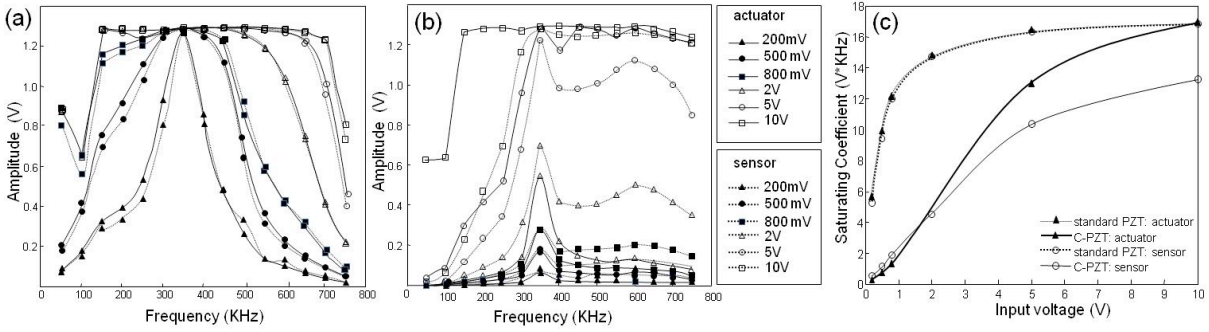
Figure 30. Stack PZT test results. (a) Standard PZT; (b) CPZT with CNTs electrode; (c) Saturating coefficient vs. input voltage for the actuating and sensing case of a standard PZT and a CPZT.

The results of the CNTs nano-electrode efficiency under ultrasonic excitation frequency can be viewed in Figure 30b for the PZT stack test setup. Figure 30(a) shows the standard PZT case for comparison. The graphs picture the maximum amplitude vs. frequency of the output signal for both sensing (dotted lines) and actuating (continuous lines) cases under increasing pick-to-pick input voltages. It is observed that, as expected, the CNTs electrode does not affect the resonance frequency of the PZT which sets its value at 350 kHz for both standard and CPZT samples. It is also observed that, in both cases, the maximum amplitudes increase with increasing input voltage and this type of response occurs for the sensing as well as for the actuating case. However it is found that standard PZTs reach their maximum charges capability (charges saturation) as soon as a 2V electrical input is applied, while the CPZTs reach their saturation level upon application of a 10V input. Moreover, while standard PZTs function very similarly in the sensing and actuating case, a slight response variation is observed for the
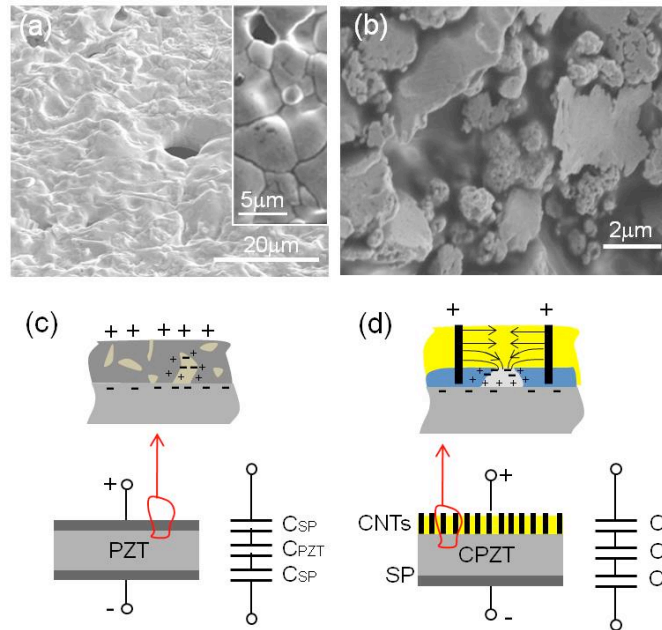
Figure 31. (a) SEM image of a SP electrode and a top view with higher magnification (inset); (b) SEM image of a CG layer; (c) schematic of the parasitic capacitance of a SP electrode; schematic of the parasitic capacitance caused by the CG layer

CPZTs. These factors can be more easily viewed in Figure 30(c) that plots the saturating coefficient vs. input voltage, being the saturating coefficient defined as the area underneath the curves plotted in Figure 30(b) and 30(c). It is worth noting that these results clearly show that the electrode efficiency of the nanoelectrode is comparable to standard PZTs for input voltages equal to or higher than 10V (maximum applicable voltage for the used signal generator) as needed for most practical applications.

The different response of CPZTs compared with standard PZTs and the different CPZTs behavior as sensor and as actuator can be explained by considering the physical nature of the nano-electrode, the CNTs conductivity and the effect of the nano-electrode on the electrical behavior of the system. When charges accumulate on the PZT surface (sensing case), these charges should be collected by the electrode in direct contact with that surface. Vice versa, in the actuating case an input voltage is applied to the PZT through the electrodes in contact with its surfaces. In both cases the electrode plays a critical role. The CNTs forest consists of a packed array of fibers with a specific inter-tube distance. The charges transfer between the PZT and the nano-electrode occurs mostly in the local areas where the CNTs tips contact the PZT grains and consequently the charges are only partially collected/transferred by the nano-electrode. This behavior is more evident at low applied voltages which lead to lower charges density on the PZT surface. With increasing input voltage, the charges density increases and a higher number of charges is collected/transferred by the CNTs electrode.

In addition to these purely physical considerations, other factors should be taken into account. For instance, the electrical conductivity of the nanotubes is known to be stronger along their longitudinal direction, however the input/output signals were applied or detected through an electrical wire which was placed in local contact with the nano-electrode. This obviously causes an increased electrical resistance of the electrode, which is not observed in the SP electrode case, which, for its physical nature, has an approximately isotropic conductivity. Again, higher voltages can reduce this effect in the nano-electrode case. Moreover, CNTs forests are characterized by a non-ohmic behavior above a threshold value. This means that their electrical resistance decreases with increasing voltage.

While all these observations clearly explain the increase of the output/input voltage amplitude with increasing input voltage in the actuator (Figure 30(b)), it is unclear why the CPZT behaves slightly differently in the sensor and the actuator case. This phenomenon can be explained by taking into consideration the circuit capacitance which is schematically depicted in Figure 31(d) for a CPZT and in Figure 30(c) for a standard PZT. In the standard PZT case, the PZT ceramic capacitance (C_{PZT}) is in series with the parasitic capacitance of the SP electrode (C_{SP}). This is because SP electrodes are often characterized by irregularly distributed voids or residual dielectric binders (Figure 31(a) and 31(c)) the latter occurring if the firing temperature is below the sintering temperature. The overall capacitance of a standard PZT is then lowered by this additional series capacitance. In the CPZT case, the PZT capacitance is in series with the parasitic CG capacitance (C_{CG}) that was used to bond the CNTs tips to the PZT and with the parasitic CNTs capacitance (C_{CNTs}) (see Figure 31(b) and 31(d)).

The results of the global electromechanical characterization of the nano-electrodes are reported in Figure 32 which shows the output amplitudes of A_0 mode and S_0 mode for the tested C-PZTs and PZTs, while Figure 33 shows the average sensor signal difference for standard PZTs and C-PZTs.
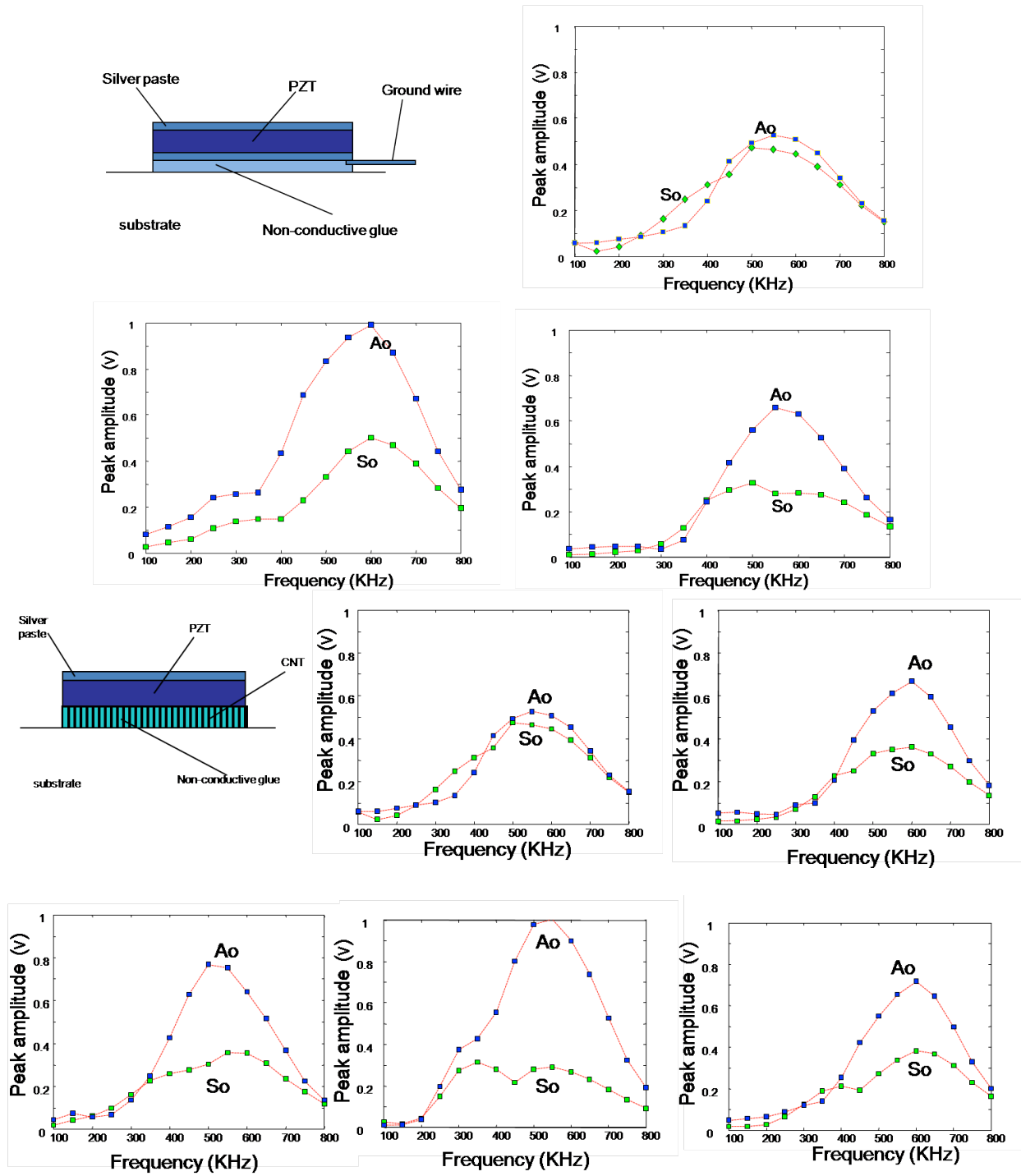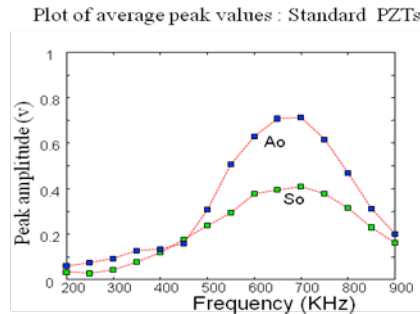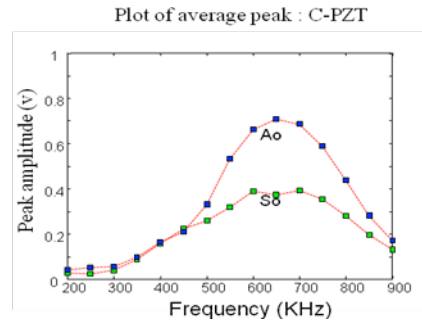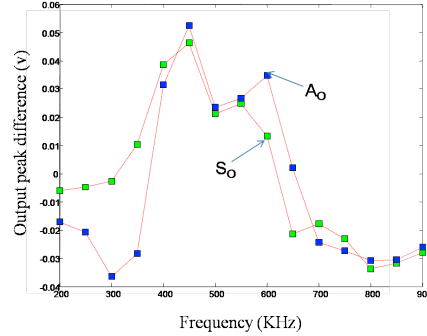
Figure 32. Output signal amplitudes of A0 mode and S0 mode for the tested PZTs and C-PZTs

(a)Average output amplitude of PZT samples

(b) Average output amplitude of C-PZT samples

(c) Average output amplitude difference between C-PZT samples and PZT samples

Figure 33. Average test result for standard PZT and C-PZT on the panel

These results show that there is no significant variation for the average output from C-PZTs and standard PZTs. In the 400 kHz to 600 kHz range, the C-PZT provides stronger signal than PZT. At about 450 kHz, the signal from C-PZT is better than the signal from PZTs (20% improvement for A_0 and S_0). However, for both PZT and C-PZT, the strongest signals both appeared at about 650 kHz, the output amplitudes were much bigger than the outputs at 450 kHz. At this frequency, the C-PZT didn't show signal improvement. When the frequency goes beyond 650 kHz, the C-PZT provided smaller signal amplitude than PZT.

8. Carbon Nanosensors for Bondline Monitoring

8.1 Problem Statement

As previously stated the ideal solution is to have, on one side, a stronger adhesive layer so as to reduce the risk of interfacial failure as well as to enhance the interface integrity over time, and, on the other side, it is necessary to monitor the health of the interface during fabrication as well as during the life-time of the SHM system. The objective of this study is to demonstrate the capability of the CPZT to monitor the bondline health of PZT sensors/actuators during bonding and once permanently mounted on a metal structure.

8.2 Our Solution to the Problems

With the help of the CPZTs' design it is here demonstrated, for the first time that it is possible to access the bondline health of PZT sensors/actuators during the in-service life of an SHM system. As previously stated, the CPZT bondline consists of an adhesive layer fully integrated with oriented CNTs (see fabrication method) that, in addition to the previously demonstrated functions, is also capable to perform the following additional functions: Step 1: adhesive cure monitoring during fabrication, and Step 2: monitor the adhesive integrity (debond/cracks or degradation) over time. The concept at the base of the monitoring capability is that the CNTs in the bondline work as an array of carbon nanosensors which, being permanently integrated into the interface, can continuously monitor the bondline health in multiple stages (from fabrication to the entire in-service life). The functional key of the proposed approach is that the electrical resistance of the carbon nanosensors, measured between the metal plate and the silver paste electrode, is here demonstrated to be affected by both the adhesive properties during curing and by the bondline integrity.

8.3 Our Approach

To demonstrate the proposed monitoring capability, the sensing response of the CPZT sensors/actuators is first investigated under static conditions to prove the capability of the proposed nanostructured bondline to detect both: adhesive curing and bondline integrity. Fatigue studies are then performed to evaluate the monitoring capability during continuous cyclic PZT actuations and structural loadings. The same tests are also performed with standard PZTs bonded to a metal structure with conductive and with non-conductive adhesive layers. This is done to prove the unique sensing capability of the proposed CPZT design.

8.4 Fabrication

A carpet of multiwalled carbon nanotubes (MWNTs) was grown with a chemical vapor deposition process using ethylene as hydrocarbon source and Fe as catalyst nanoparticles as previously described. The MWNTs were then transferred, as previously shown, by means of an ultra-thin conductive adhesive layer, onto a SMART Layer integrated with a standard PZT [27]. The SMART Layer consists of a dielectric film (Kapton HN) that hosts standard PZTs whose electrodes are interconnected to pre-patterned circuits. The resulting SMART Layers integrated with the CPZT, were then bonded to Al plates with the help of a non-conductive (NC) adhesive. Standard SMART Layers were also bonded to the Al plates by means of conductive (CG) and NC adhesives and were used as baseline sensors.

8.5 Results and Discussion

The health monitoring capability in terms of adhesive curing and debond/crack detection is first investigated (static analysis), then, the results of the fatigue study are presented to show both the effect of continuous PZT cycling (expansions and contractions) and the effects of fatigue structural loadings, on the CPZT bondline sensing capability. Figures 34a, 34b, 34c show images of the fabricated samples.

### 8.5.1 Carbon Nanosensors for Adhesive Cure Monitoring

Adhesive cure monitoring was performed by detecting the electrical resistance variation (measured between the SP electrode and the Al plate, during the curing process) of the ensemble of carbon nanosensors. The as-prepared samples (CPZTs and standard PZTs as previously described) were inserted in an oven for 110 minutes at 66°C, during which time resistance data were collected. The results can be viewed in Figure 34d where the normalized electrical resistance R/Ro vs. time is reported. The CPZT bondline is clearly extremely sensitive to epoxy curing. On the contrary, it was not possible to monitor during the curing process with standard bondlines made of CG or NC adhesives. The trend in Figure 34d can be interpreted as follows: (1) rapid viscosity decrease of the adhesive (drastic R drop); (2) adhesive cross-linking (slower R decrease until nearly constant value), (3) complete crystallization at 60 minutes (constant R), and (4) CNTs resistance decrease due to the temperature decrease. The dominant factor is that a decrease in viscosity, with the resulting bondline thinning due to fluid flows, modifies the electrical contact between the CNTs tips and the metal plate. This is caused by folding of the MWNTs tips in contact with the metal plate (as previously observed by the authors [27]). Contact resistance adjustments happen, at different rates, until full crystallization is reached. In this case a rigid CNTs tips/metal configuration characterizes the interfacial layer leading to a constant R/Ro value. These results suggest that it is possible to determine the adhesive cure level by monitoring the R/Ro ratio of the bondline during the curing process. The full adhesive cure is reached when the R/Ro value becomes a steady state. These results suggest that the CPZT has the unique capability to perform in-situ cure monitoring analysis.
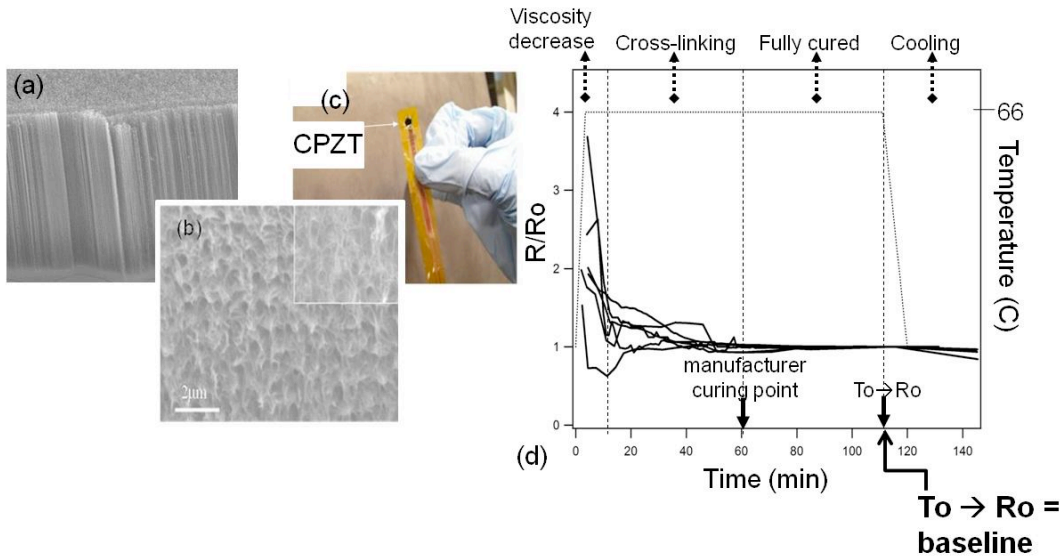
Figure 34. (a) SEM image of a carpet of MWNTs, (b) SEM image of the MWNTs in the bondline, (c) Smart layer integrated with a CPZT, (d) Cure monitoring results.

8.5.2. Carbon Nanosensors for Debond/Crack Detection (Static Analysis)

The carbon nanosensors in the CPZT bondline were also shown to be sensitive to debond/cracks that may occur between a PZT and a metal hosting structure. A small interfacial debond (8% of the unbonded area) was artificially generated in the CPZTs bondline by means of a removable rod placed underneath the bond. This artificial debond is predicted to lead to a resistance variation $\Delta R/Ro\%$ (before [*Ro*] and after [*R*] debond) of 8.7%, being the resistance $\Delta R/Ro$ approximately proportional to the ratio of the debonded area (S_{deb}) over the difference between the unbonded area and S_{deb}. The experimental CPZTs response was compared with that of the baseline cases (standard PZTs) as shown in the examples in Figure 35. The CPZTs were found to be sensitive to the generated debond/cracks with measured $\Delta R/Ro$
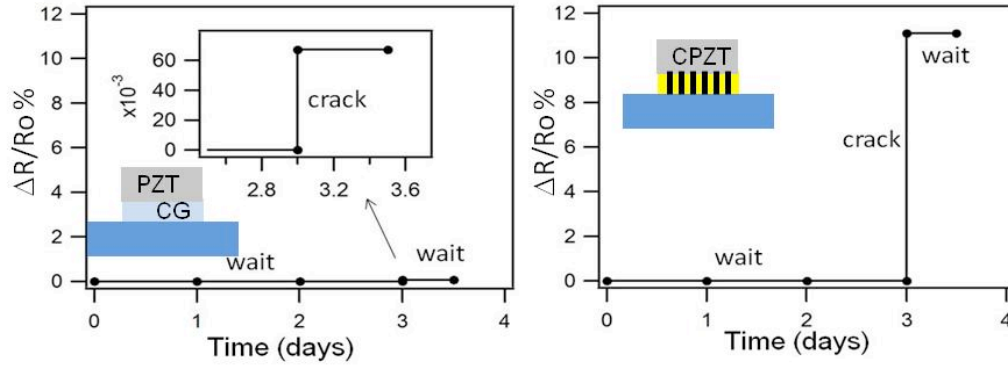
Figure 35. (Left) Debond monitoring of a standard PZT with CG adhesive (not sufficiently sensitive), (Right) Debond monitoring for the CPZT case (sensitive).

values ranging from 8.9% and up to 26.2%. These test results prove that the carbon nanosensors can detect debond/cracks generated in the bondline, and, most importantly also show, as expected, that the effective damaged area, in each of the tested samples, is larger than 8.7%. This larger area is due to the boundary effects around the removed rod. Standard PZTs, bonded to the plate with a CG layer, showed a much lower sensitivity (0.067% only) due to the extremely high conductivity of the silver-based film.

8.5.3 Bondline Monitoring Under Fatigue Loading Conditions

Tests were performed to monitor the bondline health under cyclic PZT expansions and contractions, and under fatigue structural loadings.

 8.5.3.1 Monitoring under cyclic actuation

Two CPZT sample types were studied: (1) fully bonded to an Al plate, and (2) bonded to an Al plate engineered with a movable rod to artificially induce a debond, as previously described. CPZTs were cyclically actuated (10 V, 9.8kHz) for 3 days and simultaneously the bondlines were monitored through the carbon nanosensors. The rod was then removed from one of the samples, the CPZT was left to rest for 3 days and finally it was again actuated for 43 days. The test results are shown in Figure 36. At first the resistance slowly increased in both samples, indicating loss/deterioration of the contact between the CNTs tips and the Al plate or microcracks formation; however, after the induced debond, the damaged sample had a higher increase rate in R indicating, as expected, that stress concentrations in the damaged areas enhance bondline deterioration.
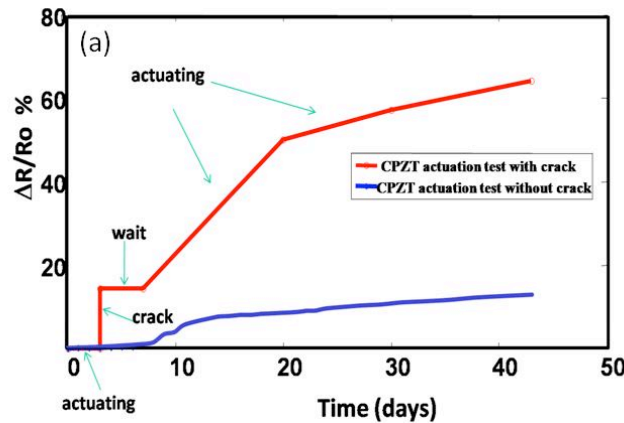
Figure 36. Monitoring during cyclic actuation.

8.5.3.2 Monitoring under fatigue structural loading

An MTS was used to fatigue an Al plate integrated with 3 CPZT samples. The CPZT bondline resistance value (example in Figure 37) was approximately constant for 1.5M cycles (under 8.9KN fatigue load and 12Hz), after which value the load was increased. As soon as the Al plate broke (at 2.2M cycles) the bondline monitoring was interrupted. A drastic resistance increase was detected through the carbon nanosensors right before the plate failure. This behavior is probably caused by the strain level increase which may also causes a partial damage in the bondline. These results clearly show that the CPZT bondline is not meaningfully affected by the cyclic structural loadings unless critical loads are applied to the hosting structure.
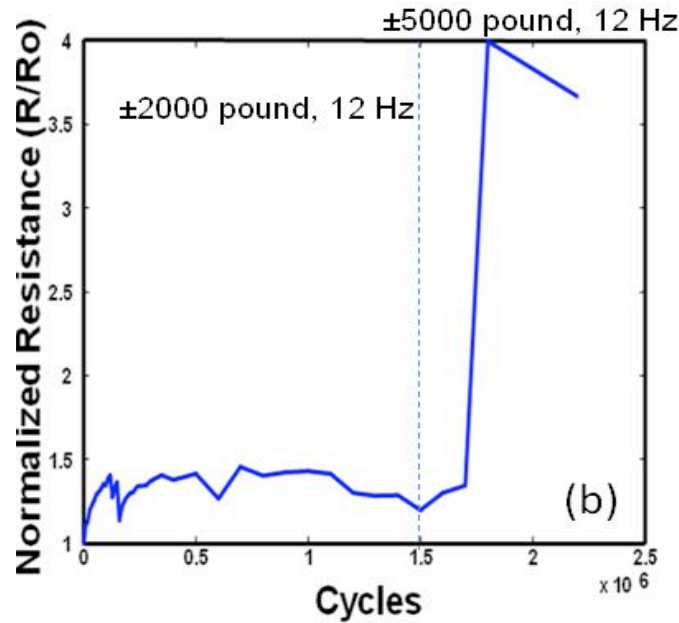

Figure 37. Monitoring during fatigue structural loadings.

9. Conclusions

A novel carbon nanotube coated piezoelectric design was presented to enhance the bondline strength of PZT sensors and actuators mounted on metal structures and to monitor, in real time, the bondline properties during adhesive curing and during the in-service life of a structure. It was shown that, the integration of oriented CNTs into the bondline can significantly improve the shear strength of the bondline and that, with the proposed CPZT design, it is possible to continuously monitor over time the adhesive curing during fabrication and the interface integrity (debond/crack) during the in-service life of the hosting structure. The here presented study has the potential to allow for the realization of the next generation of structural health monitoring systems integrated with more reliable and durable sensors and actuators.

10. References

[1] Asada H, Sotozaki T, Endoh S and Tomita T 1998 Practical evaluation of crack detection capability for visual inspection in Japan *NATO RTO Mtg Proc. 10: Airframe Inspection Reliability Under Filed/Depot Conditions* paper 15

[2] Robert Seydel and Fu-Kuo Chang, Impact identification of stiffened composite panels: II. Implementation Studies, Smart Materials and Structures, 10, 370-379, 2001

[3] Jeong-Beom Ihn and Fu-Kuo Chang, Detection and Monitoring of hidden fatigue crackgrowth using a built-in piezoelectric sensor/actuator network: Validation using riveted joints and repair patches, Smart Materials and Structures, 13, 621-630, 2004

[4] Blackshire, J.L., Giurgiutiu, V., Cooney, A., and Doane, J., "Characterization of Sensor Performance and Durability for Structural Health Monitoring Systems," Advances Sensor Technologies for Nondestructive Evaluation and Structural Health Monitoring, SPIE, Bellingham, WA, 2005

[5] Lin, M., and F.-K. Chang. 2002. "The Manufacture of Composite Structures with a Built-in Network of Piezoceramics, *Composites Science and Technologies"*, 62(7-8), 919-939.

[6] Lanzara, G., Yoon, Y., Kim, Y., Chang, F.-K. 2009." Influence of Interface Degradation on the Performance of Piezoelectric Actuators", *Journal of Intelligent Material Systems and Structures*, 20 (14), 1699-1710. doi: 10.1177/1045389X09341198

[7] Iijima, S., "Helical microtubules of graphitic carbon," Nature, 354: 56, 1991

[8] Yang, J., Hu, J.,Wang, C., Qin, Y., and Guo, Z., "Fabrication and Characterization of Soluble Multi-Walled Carbon Nanotubes Reinforced P(MMA-co-EMA) Composites," Macromolecular Materials and Engineering, 289: 829-832, 2004.

[9] Qian, D., Kickey, E.C., Andrews, R. and Rantell, T., "Load transfer and deformation mechanisms in carbon nanotube-polystyrene Composites," Applied Physics Letters, 76: 2868, 2000.

[10] Jin, L., Bower C., and Zhou, O., "Alignment of carbon nanotubes in a polymer matrix by mechanical stretching," Applied Physics Letters, 73: 1197, 1998.

[11] Ajayan, P.M., Stephan, O., Colliex, C., and Trauth D., "Aligned Carbon Nanotube Arrays Formed by Cutting a Polymer Resin-Nanotube Composite," Science, 265: 1212, 1994.

[12] Wagner, H. D., Lourie, O., Feldman, Y., and Tenne, R. "Stress-induced fragmentation of multiwall carbon nanotubes in a polymer matrix," Applied Physics Letters, 72: 188, 1998.

[13] Schadler, L. S., Giannaris S.C., and Ajayan, P.M., "Load transfer in carbon nanotube epoxy composites," Applied Physics Letters, 73: 3842, 1998.

[14] Lourie, O., and Wagner, H. D., "Transmission Electron Microscopy Observations of Fracture of Single-Wall Carbon Nanotubes under Axial Tension," Applied Physics Letters, 73: 3527, 1998.

[15] Bower, C., Rosen, R., Jin, L., Han, J., and Zhou, O., "Deformation of carbon nanotubes in nanotube-polymer composites," Applied Physics Letters, 74: 3317, 1999.

[16] Qian, D., Kickey, E. C., Andrews, R. and Rantell, T., "Load transfer and deformation mechanisms in carbon nanotube-polystyrene Composites," Applied Physics Letters, 76: 2868, 2000.

[17] Watts, P. C. P., and Hsu, W. K., "Behaviours of embedded carbon nanotubes during film cracking," Nanotechnology, 14, 5: L7-L10, 2003.

[18] Hsiao, K., Alms, J. and Advani, S. "Use of epoxy/multiwalled carbon nanotubes as adhesive to join graphite fibre reinforce polymer composite," Nanotechnology, 14: 791-793, 2003.

[19] Sandler, J., Shaer, MSP., Prasse, T., Bauhofe, W., Schulte, K. and Windle, AH., "Development of a dispersion process for carbon nanotubes in an epoxy matrix and the resulting electrical properties," Polymer, 40 (21): 5967-5971, 1999.

[20] Koratkar, N. A., Bingqng, W., and Ajayan, M. P., "Multifunctional structural reinforcement featuring carbon nanotube films," Composites Science and Technology, 63, 1525-1531, 2003.

[21] Suhr, J., Koratkar, N., Keblinski, P., and Ajayan, P., "Viscoelasticity in carbon nanotube composites," Nature Materials, 4, 134-137, 2005.

[22] P.M. Ajayan, L.S. Shadler, C. Giannaris, A. Rubio, Adv. Mat. 12, 750, 2000

[23] P.M. Ajayan, O. Stephan, C. ColliexD. Trauth, Science, 265, 1212, 1994

[24] Q. Q. Li, M. Zaiser, V. Koutsos, Phys. Status Solidi A, 201, R89, 2004

[25] J. Zhu, H. Peng, F. Rodriguez-Macias, J. L. Margrave, V. N. Khabashesku, A. M. Imam, K. Lozano, E. V. Barrera, *Adv. Funct. Mater, 14*, 643, 2004.

[26] V. P. Veedu, A. Cao, X. Li, K. Ma, C. Soldano, S. Kar, P. M. Ajayan, M. N. Ghasemi-Nejhad, Multifunctional composites using reinforced laminae with carbon-nanotube forests, 5, 457, 2006

[27] Lanzara, G. and F.-K. Chang (2009). Design and Characterization of a carbon nanotube-reinforced adhesive coating for piezoelectric ceramic discs, *Smart Materials and Structures*, 18, 125001, doi: 10.1088/0964-1726/18/12/125001

[28] Lanzara, G. and L. Zhang (2011). Carbon Nanotube Coated Piezoelectric Actuator Under Ultrasonic Actuation Frequencies, *Nanotechnologies*, submitted

[29] Lanzara G., L. Zhang and F.-K. Chang, Carbon Nanosensors for Health Monitoring of PZT Bondline During Curing and Its In-Service Life, EWSHM2010, Sorrento 2010.

[30] Lanzara G Realization and analysis of carbon nanotube carpet microstructures 2005 *PhD Thesis (University of Rome "La Sapienza," Rome)*

[31] Lanzara G, Yoon Y and Chang F-K Carbon nanotube growth on piezoceramic substrates Unpublished